patients with previously treated metastatic breast cancer. J Clin Oncol 23:792–799
5. Vredenburgh JJ, Desjardins A, Herndon JE IId, Marcello J, Reardon DA, Quinn JA, Rich JN, Sathornsumetee S, Gururangan S, Sampson J, Wagner M, Bailey L, Bigner DD, Friedman AH, Friedman HS (2007) Bevacizumab plus irinotecan in recurrent glioblastoma multiforme. J Clin Oncol 25:4722–4729
6. Gonzalez J, Kumar AJ, Conrad CA, Levin VA (2007) Effect of bevacizumab on radiation necrosis of the brain. Int J Radiat Oncol Biol Phys 67:323–326
7. Torcuator R, Zuniga R, Mohan YS, Rock J, Doyle T, Anderson J, Gutierrez J, Ryu S, Jain R, Rosenblum M, Mikkelsen T (2009) Initial experience with bevacizumab treatment for biopsy confirmed cerebral radiation necrosis. J Neurooncol 94:63–68
8. Levin VA, Bidaut L, Hou P, Kumar AJ, Wefel JS, Bekele N, Prabhu S, Loghin M, Gilbert MR, Jackson EF (2010) Randomized double-blind placebo-controlled trial of bevacizumab therapy for radiation necrosis of the central nervous system. Int J Radiat Oncol Biol Phys. doi:10.1016/j.ijrobp.2009.12.061
9. Miyashita M, Miyatake S, Imahori Y, Yokoyama K, Kawabata S, Kajimoto Y, Shibata MA, Otsuki Y, Kirihata M, Ono K, Kuroiwa T (2008) Evaluation of fluoride-labeled boronophenylalanine-PET imaging for the study of radiation effects in patients with glioblastomas. J Neurooncol 89:239–246
10. Miyatake S, Kawabata S, Nonoguchi N, Yokoyama K, Kuroiwa T, Matsui H, Ono K (2009) Pseudoprogression in boron neutron capture therapy for malignant gliomas and meningiomas. Neurooncology 11:430–436
11. Miyatake S, Kawabata S, Kajimoto Y, Aoki A, Yokoyama K, Yamada M, Kuroiwa T, Tsuji M, Imahori Y, Kirihata M, Sakurai Y, Masunaga S, Nagata K, Maruhashi A, Ono K (2005) Modified boron neutron capture therapy for malignant gliomas performed using epithermal neutron and two boron compounds with different accumulation mechanisms: an efficacy study based on findings on neuroimages. J Neurosurg 103:1000–1009
12. Kawabata S, Miyatake SI, Kuroiwa T, Yokoyama K, Doi A, Iida K, Miyata S, Nonoguchi N, Michiue H, Takahashi M, Inomata T, Imahori Y, Kirihata M, Sakurai Y, Maruhashi A, Kumada H, Ono K (2009) Boron neutron capture therapy for newly diagnosed glioblastoma. J Radiat Res (Tokyo) 50:51–60
13. Fitzek MM, Thornton AF, Rabinov JD, Lev MH, Pardo FS, Munzenrider JE, Okunieff P, Bussiere M, Braun I, Hochberg FH, Hedley-Whyte ET, Liebsch NJ, Harsh GR IV (1999) Accelerated fractionated proton/photon irradiation to 90 cobalt gray equivalent for glioblastoma multiforme: results of a phase II prospective trial. J Neurosurg 91:251–260
14. Iuchi T, Hatano K, Narita Y, Kodama T, Yamaki T, Osato K (2006) Hypofractionated high-dose irradiation for the treatment of malignant astrocytomas using simultaneous integrated boost technique by IMRT. Int J Radiat Oncol Biol Phys 64:1317–1324
15. Delanian S, Balla-Mekias S, Lefaix JL (1999) Striking regression of chronic radiotherapy damage in a clinical trial of combined pentoxifylline and tocopherol. J Clin Oncol 17:3283–3290
16. Glantz MJ, Burger PC, Friedman AH, Radtke RA, Massey EW, Schold SC Jr (1994) Treatment of radiation-induced nervous system injury with heparin and warfarin. Neurology 44:2020–2027
17. Rizzoli HV, Pagnanelli DM (1984) Treatment of delayed radiation necrosis of the brain. A clinical observation. J Neurosurg 60:589–594
18. Shaw PJ, Bates D (1984) Conservative treatment of delayed cerebral radiation necrosis. J Neurol Neurosurg Psychiatry 47: 1338–1341
19. Tandon N, Vollmer DG, New PZ, Hevezi JM, Herman T, Kagan-Hallet K, West GA (2001) Fulminant radiation-induced necrosis after stereotactic radiation therapy to the posterior fossa. Case report and review of the literature. J Neurosurg 95:507–512
20. Coderre JA, Morris GM, Micca PL, Hopewell JW, Verhagen I, Kleiboer BJ, van der Kogel AJ (2006) Late effects of radiation on the central nervous system: role of vascular endothelial damage and glial stem cell survival. Radiat Res 166:495–503
21. Kimura T, Sako K, Tohyama Y, Aizawa S, Yoshida H, Aburano T, Tanaka K, Tanaka T (2003) Diagnosis and treatment of progressive space-occupying radiation necrosis following stereotactic radiosurgery for brain metastasis: value of proton magnetic resonance spectroscopy. Acta Neurochir (Wien) 145:557–564
22. Midgley R, Kerr D (2005) Bevacizumab—current status and future directions. Ann Oncol 16:999–1004

Applied Radiation and Isotopes 69 (2011) 1721–1724

Contents lists available at ScienceDirect

Applied Radiation and Isotopes

journal homepage: www.elsevier.com/locate/apradiso

Boron neutron capture therapy for clear cell sarcoma (CCS): Biodistribution study of *p*-borono-L-phenylalanine in CCS-bearing animal models

T. Andoh [a], T. Fujimoto [b], T. Sudo [c], I. Fujita [b], M. Imabori [b], H. Moritake [d], T. Sugimoto [e], Y. Sakuma [f], T. Takeuchi [g], S. Kawabata [h], M. Kirihata [i], T. Akisue [j], K. Yayama [k], M. Kurosaka [j], S. Miyatake [h], Y. Fukumori [a], H. Ichikawa [a,*]

[a] *Laboratory of Pharmaceutical Technology, Faculty of Pharmaceutical Sciences and Cooperative Research Center of Life Sciences, Kobe Gakuin University, Kobe 650-8586, Japan*
[b] *Department of Orthopaedic Surgery, Hyogo Cancer Center, Akashi 673-0021, Japan*
[c] *Section of Translational Research, Hyogo Cancer Center, Akashi 673-0021, Japan*
[d] *Department of Pediatrics, Miyazaki University, Kiyotake 889-1692, Japan*
[e] *Department of Pediatrics, Saiseikai Shigaken Hospital, Ritto 520-3046, Japan*
[f] *Department of Pathology, Hyogo Cancer Center, Akashi 673-0021, Japan*
[g] *Department of Pathology, Kochi University, Nangoku 783-8505, Japan*
[h] *Department of Neurosurgery, Osaka Medical College, Osaka 569-8686, Japan*
[i] *Graduate School of Life and Environmental Sciences, Osaka Prefecture University, Sakai 599-8531, Japan*
[j] *Department of Orthopaedic Surgery, Kobe University Graduate School of Medicine, Kobe 650-0017, Japan*
[k] *Laboratory of Cardiovascular Pharmacology, Faculty of Pharmaceutical Sciences and Cooperative Research Center of Life Sciences, Kobe Gakuin University, Kobe 650-8586, Japan*

ARTICLE INFO

Available online 1 March 2011

Keywords:
Biodistribution
p-Borono-L-phenylalanine
Clear cell sarcoma
MP-CCS-SY
Boron neutron capture therapy
Anti-BPA monoclonal antibody

ABSTRACT

Clear cell sarcoma (CCS) is a rare melanocytic malignant tumor with a poor prognosis. Our previous study demonstrated that *in vitro* cultured CCS cells have the ability to highly uptake L-BPA and thus boron neutron capture therapy could be a new option for CCS treatment. This paper proved that a remarkably high accumulation of ^{10}B (45–74 ppm) in tumor was obtained even in a CCS-bearing animal with a well-controlled biodistribution followed by intravenous administration of L-BPA-fructose complex (500 mg BPA/kg).

1. Introduction

Clear cell sarcoma (CCS), a rare melanocytic malignant tumor with a predilection for young adults, is of poor prognosis. Since its treatment other than surgical resection is lacking, a new clinical approach for its management is required (Weiss and Goldblum, 2001).

Melanoma cells preferentially take up *p*-borono-L-phenylalanine (L-BPA) because its chemical structure is similar to tyrosine required for melanogenesis. Therefore, L-BPA has been used in boron neutron capture therapy (BNCT) for malignant melanoma (Mishima et al., 1989). CCS is also capable of producing melanin. Similarity in melannogensis between melanoma and CCS promises high BPA uptake by CCS. Indeed, we have proved that remarkable uptake of BPA with an extremely high level, i.e., 80 μg ^{10}B/g cells, took place when CCS was exposed to BPA-containing cell culture medium *in vitro* (Fujimoto et al., in press). Thus, BNCT using L-BPA is expected to be a new clinical option for the treatment of CCS, provided that such a high accumulation of boron in CCS can be realized even in vivo under a well-controlled biodistribution of L-BPA.

In the present study, we are aiming at investigating *in vivo* biodistribution of L-BPA in a CCS-bearing animal model. For this purpose, CCS cell line of human origin (MP-CCS-SY) was employed and a CCS-bearing animal model was established by subcutaneous transplantation of MP-CCS-SY to nude mice. Biodistribution of L-BPA followed by its intravenous administration into the CCS-bearing nude mice thus obtained was evaluated. Additionally, the tumor resected from the BPA-given mice was assessed with immunohistological examination using anti-BPA monoclonal antibody to visualize microscopic distribution of BPA in the tumor tissue.

2. Materials and methods

2.1. Chemicals

L-BPA (^{10}B enriched) was kindly supplied by Stella Pharma Corporation (Osaka, Japan). Fructose, perchloric acid ($HClO_4$, 60%),

* Corresponding author. Tel.: +81 78 974 1551; fax: +81 78 974 4814.
E-mail address: ichikawa@pharm.kobegakuin.ac.jp (H. Ichikawa).

0969-8043/$ - see front matter © 2011 Elsevier Ltd. All rights reserved.
doi:10.1016/j.apradiso.2011.02.005

hydrogen peroxide (H_2O_2, 30%) and boron standard solution (1000 μg/mL) were purchased from Nacalai Tesque, Inc. (Kyoto, Japan). L-BPA was used as a fructose complex (BPA-Fr, 4000 μg ^{10}B/mL) (Yoshino et al., 1989). Anti-BPA monoclonal antibody (anti-BPA MAb) was obtained as a self-made product (Kirihata and Asano 2008). LSAB2 kit/HRP (DAB) was purchased from DAKO Japan, Inc. (Kyoto, Japan).

2.2. Cell

The MP-CCS-SY established from the bone metastatic tissue of a 17-years-old girl was employed as a human CCS cell line (Moritake et al., 2002). The melanogenesis of MP-CCS-SY has been reported previously: the melanosome was identified by electron-microscopic appearance and indirect immunofluorescence for melanoma-associated antigens (Moritake et al., 2002). The MP-CCS-SY cells were cultured in RPMI-1640 medium containing penicillin (100 U/mL), streptomycin (100 μg/mL) and 10% heat-inactivated fetal bovine serum, and incubated in a humidified atmosphere of 5% CO_2 in air at 37 °C.

2.3. Animal and tumor

All animal experiments were performed according to the regulations of the Animal Care and Use Committee of Kobe Gakuin University (Kobe, Japan). Four-weeks-old female BALB/cAJcl-nu/nu nude mice (body weight of approx. 15 g) were purchased from CLEA Japan, Inc. In order to establish CCS-bearing animal models, 0.1 mL of the culture medium containing 1×10^7 MP-CCS-SY cells was subcutaneously (s.c.) implanted into the dorsal or femoral region of the nude mice. These two models were used in biodistibution studies of L-BPA.

2.4. Biodistribution of BPA-Fr

When the MP-CCS-SY tumor in each mouse (body weight of approximately 20 g) grew to about 10 mm in diameter (approximately four weeks after MP-CCS-SY cells implantation), BPA-Fr (500 mg BPA/kg) was intravenously (i.v.) administered via

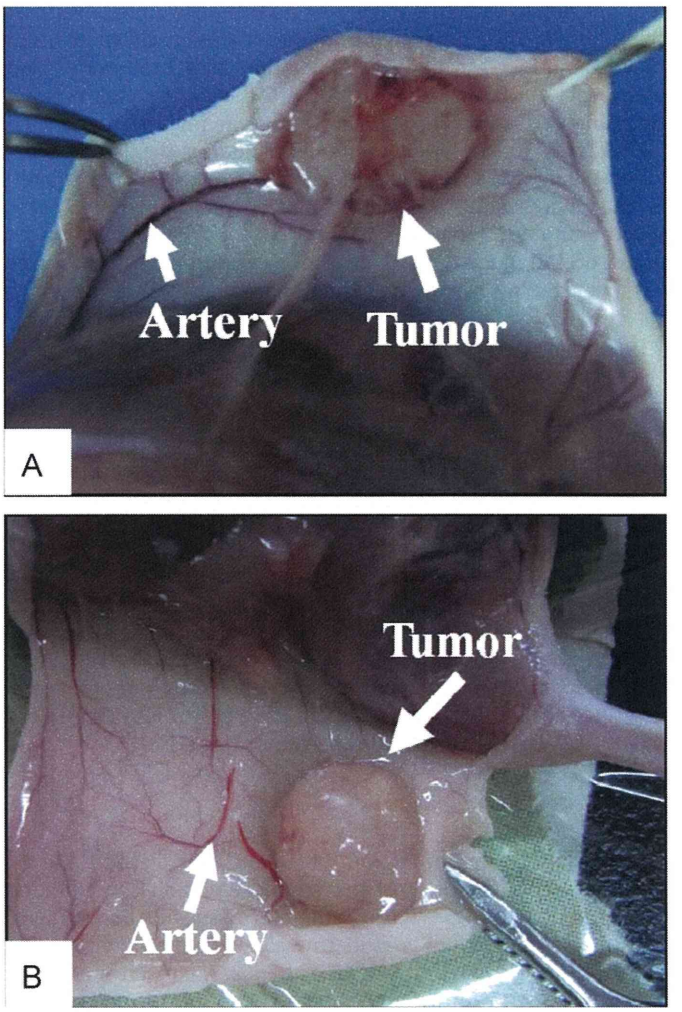

Fig. 2. Photographs showing CCS formation in dorsal region (A, Fujimoto et al., in press) and femoral region (B) of nude mice. Significant angiogenesis can be seen especially in the dorsal region.

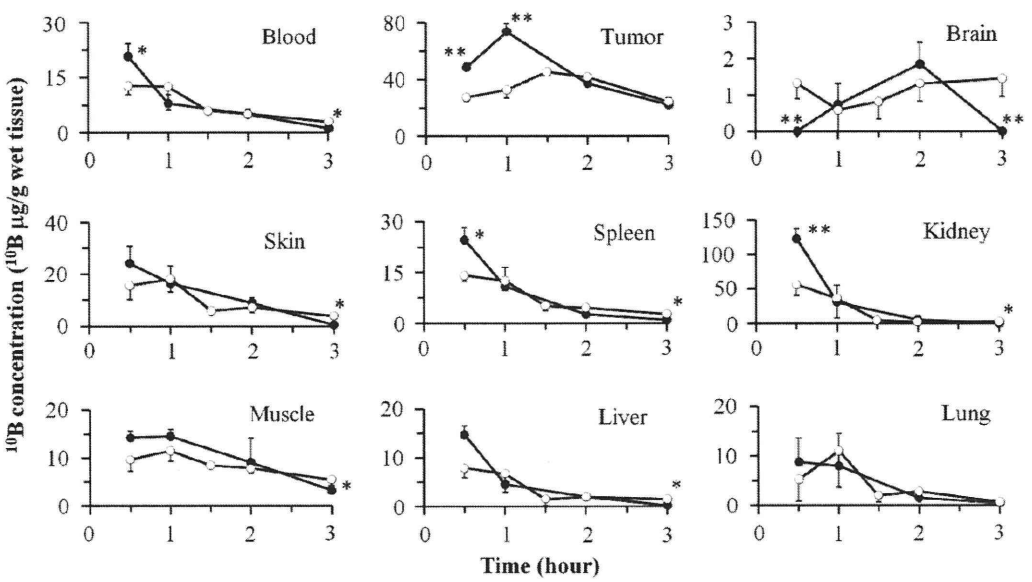

Fig. 1. Time course changes of ^{10}B concentration in tissues after i.v. administration of BPA-Fr (500 mg BPA/kg) to nude mice having MP-CCS-SY in dorsal region (●) and those in femoral region (○). *: $p < 0.05$, **: $p < 0.01$, significantly different from the ^{10}B concentration of dorsal region. Each value represents the mean ± S.D. ($n=3$).

femoral vein to each tumor-bearing nude mouse under anesthesia with diethyl ether. At predetermined time intervals after dosing, blood sample was collected by cardiac puncture under deep anesthesia and then residual blood in the organs was removed by saline perfusion. Subsequently, the nude mice were sacrificed with diethyl ether. Tissue samples including the liver, spleen, kidney, lung, brain and tumor were collected immediately, washed with saline and lightly blotted to remove any excess blood and water. The skin and muscle were collected from the nates of the mice. The liver, kidney, brain and tumor were homogenized by a high-speed homogenizer.

2.5. Histological evaluation

The tumor mass was resected from the dorsally MP-CCS-SY-bearing nude mouse sacrificed one hour after intravenous administration of BPA-Fr (500 mg BPA/kg) under anesthesia with diethyl ether. This mass was routinely processed by fixation in formalin for overnight at 20–23 °C and then embedded in paraffin. Serial tissue sections were cut from the paraffin block, placed on glass slides and dried overnight. A part of the sections was stained with hematoxylin–eosin (H.E.) according to standard protocols for histological examination. Separately, some of the sections were incubated with anti-BPA Mab, stained with LSAB2 kit/HRP (DAB) and then counterstained with hematoxylin by the procedure described in the literature (Nakagawa, 2006) to visualize microscopic distribution of L-BPA in the tumor tissues.

2.6. Determination of boron

Quantitative determination of boron was carried out by the inductively coupled plasma atomic emission spectrometric (ICP-AES) method. A weighed sample of tissues or homogenates (typically 100–200 mg) was hermetically digested with $HClO_4$ (0.6 mL) and H_2O_2 (1.2 mL) for 48 h at 75 °C. The resulting solution was diluted with ultra pure water to be 5 mL in total volume, followed by filtration with a 0.45 μm disposable filter unit. Boron concentration in each sample was determined by ICP-AES (SPS 3100, SII NanoTechnology Inc., Tokyo, Japan). The emission intensity was measured at 249.773 nm. The calibration curve obtained from dilutes of the boron standard solution (1000 μg/mL) was linear in the range of 0.2–10 μg/mL.

3. Results and discussion

The biodistribution data of boron after i.v. administration of BPA-Fr (500 mg BPA/kg) are shown in Fig. 1. As a general tendency, the boron concentrations in blood, spleen, kidney, liver and skin decreased rapidly after i.v. administration of BPA-Fr. The peak boron concentrations did not exceed 25 μg ^{10}B/g in the liver, spleen, brain, lung, muscle and skin, while the transiently high boron concentration was found in kidney. In contrast, the boron concentration in tumor increased rapidly, peaked at 1 or 1.5 hours, and subsequently decayed with time. The peak concentration reached 74 μg ^{10}B/g wet tumor tissue (ppm) for dorsally tumor-bearing mice and 45 ppm for femorally tumor-bearing mice, respectively (Fig. 1). This concentration was higher than the minimum effective concentration of boron, i.e., 20–30 μg ^{10}B/g (Barth et al., 1992) in BNCT. Such a high boron concentration in the CCS-bearing animals would be attributable to a high cell-uptake and/or cell-affinity of L-BPA (Fujimoto et al., in press).

The dorsally tumor-bearing mice showed significantly higher peak boron concentrations in tumor, compared with the femorally tumor-bearing mice (Fig. 1). As represented in Fig. 2, the CCS in dorsal region resulted in somewhat more distinct angiogenesis than the CCS in femoral region. This difference in the extent of angiogenesis may account for the higher boron concentration in dorsally tumor-bearing mice.

Both tumor-to-blood (T/B) and tumor-to-skin (T/S) ratios should be large enough in order to avoid radiobiological damage to the normal skin. The T/B and T/S ratios at 1 hour after administration of BPA-Fr in dorsally tumor-bearing mice were 9.2 and 4.5, respectively, while those at 1.5 hour after administration of

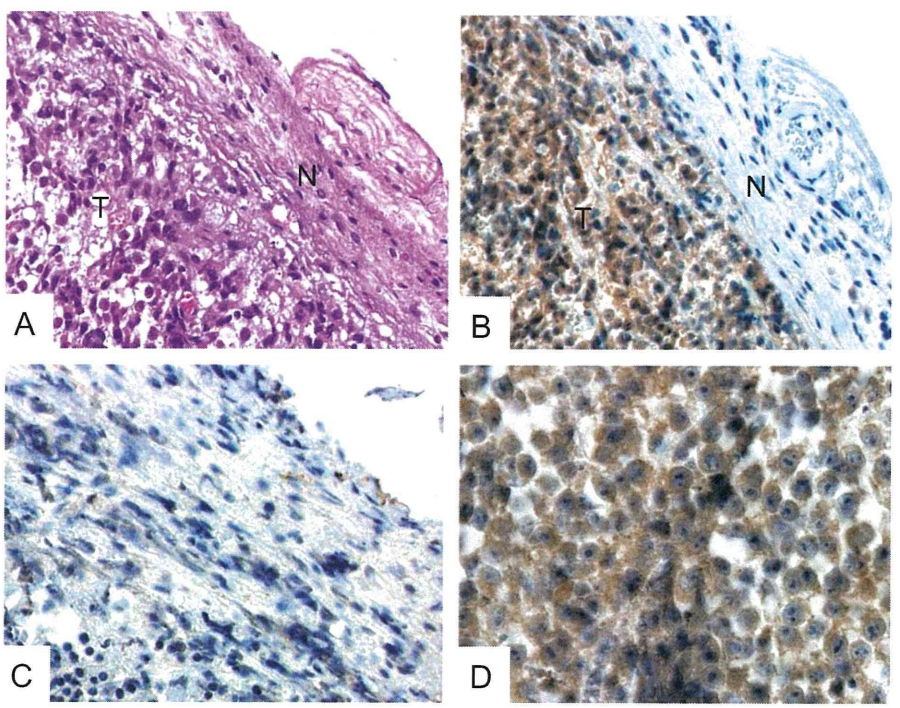

Fig. 3. Micrographs (100 ×) showing tumor sections (T) with the surrounding normal tissues (N) resected from BPA-administered mice (A, B, D) and non-BPA-administered mice (negative control, C). A: Hematoxylin-Eosin staining; B-D: immunostaining with anti-BPA MAb. D represents a magnified image (× 400) of B.

BPA-Fr in femorally tumor-bearing mice were 7.6 and 7.8, respectively. Previous experimental and clinical studies suggested that these ratios have to be at least 3 (Barth et al., 1996). The values of T/B and T/S obtained in the present study fulfill the therapeutic requirements.

H.E. staining data revealed that CCS tumor tissues were histologically different from the surrounding normal tissues, as evidenced from Fig. 3A. Fig. 3B–D shows the results of immunostaining with anti-BPA MAb. Here, the presence of BPA can be detected by browny coloration of tissues. The accumulation of BPA indicated by brownish color was predominant in the tumor tissues over the surround normal tissues (Fig. 3B), and tumor tissues obtained without BPA administration (negative control) did not develop brownish color well (Fig. 3C), suggesting that BPA is likely to be distributed in a CCS-selective manner. Interestingly, BPA was detected mainly in intracellular regions of CCS as seen in the magnified photograph (Fig. 3D). This can be a strong indication of cellular uptake of BPA taking place even *in vivo* CCS-bearing animals. Further studies are warranted to determine whether melanin synthesis is related to the high accumulation of boron in CCS.

4. Conclusions

Biodistribution of boron after i.v. administration of BPA-Fr into newly established CCS-bearing nude mice was studied. The peak concentrations of boron in tumor varied from 45 to 74 ppm, depending on the animal models. The T/B and T/S ratios were 9.2 and 4.5 in dorsally tumor bearing model, and 7.6 and 7.8 in femorally tumor bearing model, respectively. Tumor-specific BPA distribution was microscopically observed in the intravenously BPA-Fr-given CCS-bearing mice through immunohistological examination. A preclinical BNCT trial using a CCS-bearing mouse will be a next issue to clarify whether BNCT using BPA-Fr can be a promising therapeutic option for the CCS.

Acknowledgments

This work was supported in part by a Grant-in-Aid for Scientific Research (No. 22591657) from Japan Society for the Promotion of Science.

References

Barth, R.F., Soloway, A.H., Fairchild, R.G., Brugger, R.M., 1992. BNCT for cancer-realities and prospects. Cancer 70, 2995–3007.

Barth, R.F., Soloway, A.H., Brugger, R.M., 1996. Boron neutron capture therapy of brain tumors: past history, current status and future potential. Cancer Invest. 14, 534–560.

Fujimoto, T., Andoh, T., Sudo, T., Fujita, I., Imabori, M., Moritake, H., Sugimoto, T., Sakuma, Y., Takeuchi, T., Sonobe, H., Epstein, A.L., Akisue, T., Kirihata, M., Kurosaka, M., Fukumori, Y., Ichikawa, H. Evaluation of BPA uptake in clear cell sarcoma (CCS) *in vitro* and development of an *in vivo* model of CCS for BNCT studies. Appl. Radiat. Isots., in press, doi:10.1016/j.apradiso.2011.02.006.

Kirihata, M., Asano, T., 2008. JP Patent Pending 2008-94729.

Mishima, Y., Honda, C., Ichihashi, M., Obara, H., Hiratsuka, J., Fukuda, H., Karashima, H., Kobayashi, T., Kanda, K., Yoshino, K., 1989. Treatment of malignant-melanoma by single thermal-neutron capture therapy with melanoma-seeking B-10-compound. Lancet 12, 388–389.

Moritake, H., Sugimoto, T., Asada, Y., Yoshida, A.M., Maehara, Y., Epstein, L.A., Kuroda, H., 2002. Newly established clear cell sarcoma (malignant melanoma of soft parts) cell line expressing melanoma-associated Melan-A antigen and overexpressing C-MYC oncogene. Cancer Genet. Cytogenet. 135, 48–56.

Nakagawa, N., 2006. Therapeutic effect of boron neutron capture therapy on malignant glioma: fundamental studies using C6 rat glioma models. Med. J. Kinki Univ. 31, 215–224.

Weiss, S.W., Goldblum, J.R., 2001. Enzinger and Weiss's Soft Tissue Tumors, fourth ed., pp. 1240–1250.

Yoshino, K., Suzuki, A., Mori, Y., Kakihana, H., Honda, C., Mishima, Y., Kobayashi, T., Kanda, K., 1989. Improvement of solubility of p-boronophenylalanine by complex formation with monosaccharides. Strahlenther. Onkol. 165, 127–129.

J Neurosurg 116:574–580, 2012

Slower growth of skull base meningiomas compared with non–skull base meningiomas based on volumetric and biological studies

Clinical article

Naoya Hashimoto, M.D., Ph.D.,[1] Carter S. Rabo, M.D.,[1] Yoshiko Okita, M.D., Ph.D.,[1] Manabu Kinoshita, M.D., Ph.D.,[1] Naoki Kagawa, M.D., Ph.D.,[1] Yasunori Fujimoto, M.D., Ph.D.,[1] Eiichi Morii, M.D., Ph.D.,[2] Haruhiko Kishima, M.D., Ph.D.,[1] Motohiko Maruno, M.D., Ph.D.,[3] Amami Kato, M.D., Ph.D.,[4] and Toshiki Yoshimine, M.D., Ph.D.[1]

Departments of [1]Neurosurgery and [2]Pathology, Osaka University Graduate School of Medicine, Suita; [3]Department of Neurosurgery, Osaka Prefectural Center for Adult Diseases, Osaka; and [4]Department of Neurosurgery, Kinki University School of Medicine, Sayama, Japan

Object. The precise natural history of incidentally discovered meningiomas (IDMs) remains unknown. It has been reported that for symptomatic meningiomas, tumor location can be used to predict growth. As to whether the same is true for IDMs has not been reported. This study aims to answer this question and provide biological evidence for this assumption by extending the study to involve symptomatic cases.

Methods. A total of 113 IDMs were analyzed by fine volumetry. A comparison of growth rates and patterns between skull base and non–skull base IDMs was made. Subsequently, materials obtained from 210 patients with symptomatic meningiomas who were treated in the authors' hospital during the same period were included for a biological comparison between skull base and non–skull base tumors using the MIB-1 index.

Results. The 110 patients with IDMs included 93 females and 17 males, with a mean follow-up period of 46.9 months. There were 38 skull base (34%) and 75 non–skull base (66%) meningiomas. Forty-two (37%) did not exhibit growth of more than 15% of the volume, whereas 71 (63%) showed growth. Only 15 (39.5%) of 38 skull base meningiomas showed growth, whereas 56 (74.7%) of 75 non–skull base meningiomas showed growth ($p = 0.0004$). In the 71 IDMs (15 skull base and 56 non–skull base), there was no statistical difference between the 2 groups in terms of mean age, sex, follow-up period, or initial tumor volume. However, the percentage of growth ($p = 0.002$) was significantly lower and the doubling time ($p = 0.008$) was significantly higher in the skull base than in the non–skull base tumor group. In subsequently analyzed materials from 94 skull base and 116 non–skull base symptomatic meningiomas, the mean MIB-1 index for skull base tumors was markedly low (2.09%), compared with that for non–skull base tumors (2.74%; $p = 0.013$).

Conclusions. Skull base IDMs tend not to grow, which is different from non–skull base tumors. Even when IDMs grow, the rate of growth is significantly lower than that of non–skull base tumors. The same conclusion with regard to biological behavior was confirmed in symptomatic cases based on MIB-1 index analyses. The authors' findings may impact the understanding of the natural history of IDMs, as well as strategies for management and treatment of IDMs and symptomatic meningiomas. *(DOI: 10.3171/2011.11.JNS11999)*

Key Words • **incidentally discovered meningioma** • **volumetric analysis** • **skull base** • **MIB-1 index** • **management strategy** • **oncology**

Meningiomas have increasingly been detected incidentally due to advances in neuroimaging, such as CT and MR imaging.[9] Neurological examinations and neuroradiological screening for indefinite complaints also contribute to this increase in detection, especially in advanced countries.[17] Although most IDMs can be cured surgically,[18] the morbidity and mortality associated with surgery itself cannot be determined as these tumors are generally considered asymptomatic and benign.[9] Therefore, determining the proper management for these cases is critical. However, due to the lack of knowledge regarding the exact natural history of these tumors and their potential for growth, what to consider as "appropriate" treatment remains controversial.[14]

Several authors have investigated the natural history of IDMs.[3,4,9,14,16,23,24] They have identified various factors predictive of tumor growth; however, these factors differ from study to study. Recently, we analyzed 70 IDMs using a volumetric method with a relatively long follow-up period. We concluded that most IDMs do not seem to grow for a certain period of time, and that they do not always

Abbreviation used in this paper: IDM = incidentally discovered meningioma.

grow exponentially but rather exhibit complex patterns of growth.[6] In addition, the presentation of calcification on CT or MR imaging has a negative impact on its growth.

We further surveyed other factors predictive of IDM growth, and we identified tumor location, that is, non–skull base versus skull base, as a potentially useful clinicoradiological predictor of the growth behavior of IDMs. Here, we report our results and discuss biological evidence to support these findings through expansion of the theory involving symptomatic meningiomas.

Methods

A total of 110 patients with IDMs, who are being followed up at our institution, were included in this study. The tumor growth rate of individual IDMs was analyzed using a manual volumetric method. Then, to confirm the biological differences between skull base and non–skull base tumors, 210 symptomatic patients with Grade I meningiomas, based on the WHO 2007 classification, who were treated in Osaka University Hospital, were also included. This study was approved by the ethics review board of the university.

Definition of Tumor Location

The location of the origin of the meningioma was carefully determined on MR images by N.H. and at least one of the coauthors, who are all experienced neurosurgeons (M.K., N.K., Y.F., and T.Y.). For large tumors, for which the origin is difficult to define, the most widely attached portion of the tumor in the skull was considered. In this study, we divided tumor location into 2 groups: skull base and non–skull base. Skull base origins included the olfactory groove, planum sphenoidale, cavernous sinus, sphenoid wing, clinoidal portion, tuberculum sellae, clivus, and petrous bone. Tentorial meningiomas were considered non–skull base lesions.

Volumetric Analysis of Tumor Size and Evaluation of Growth by Regression Analysis in IDMs

Between 1993 and 2009 at Osaka University Hospital, 121 patients (19 men and 102 women) were incidentally diagnosed as harboring intracranial meningiomas on the basis of MR imaging findings. We reviewed each patient's records and judged whether the tumors were totally asymptomatic or if the patient had any symptoms that could be attributed to the lesion. Meningiomas were radiologically diagnosed by the presence of an extraaxial mass, with broad-based attachment along the dura mater or with attachment to the choroid plexus in the ventricles, which were homogeneously and markedly enhanced with contrast medium as previously described.[24] Of the 121 patients, 110 who underwent MR imaging at least 3 times over the course of more than 1 year were included in this study. The results of serial MR imaging studies and clinical characteristics such as sex, age, and length of follow-up were reviewed.

Volumetric analysis and evaluation of the pattern of growth with regression analysis were conducted as previously reported.[6] Briefly, the tumor size was evaluated by volumetric assessment (volumetry) using Scion Image for Windows software (Scion Corp.). The enhanced area of the tumor in each slice image was measured by manual tracing of the tumor boundaries, and then the sum of the enhanced areas was multiplied by the slice interval of the MR imaging series. The absolute growth rate (cm^3/year) and relative growth rate (%/year) were calculated for each tumor, according to the equation described elsewhere.[14] The percentage of growth (growth volume/initial tumor volume) was calculated as well.

Inaccuracy of measurement from 2 sources of errors (one caused by using an MR imaging series with thick slice intervals and the other by manual tracing of the tumor) were addressed. For the former, we described a preliminary study with 10 cases and showed that volumetry with an MR imaging series using 6.0-mm slice intervals was estimated to show acceptable accuracy for evaluating tumor volume, compared with an MR imaging series using 2.0-mm slice intervals in the same patients.[6] This preliminary study revealed that a change in tumor volume (a percentage of growth or reduction in volume) less than 15% can be thought of as representing a measurement error. To offset the second source of measurement error, we evaluated 70 IDMs and measured them 3 times. We found that the obtained values 2 standard deviations from the calculated measurements corresponded to a change of less than 15% in each tumor volume. Considering the results from these validation studies, the cutoff for tumor growth or reduction in volume was set to 15% in this study.

The time-volume curves were plotted for each tumor, and regression analysis was performed for the group with growth. Growth curves were fitted to both exponential growth and linear growth as previously reported.[6] Regression coefficients were calculated for each regression analysis and examined statistically for significance. If the growth curve fit both exponential and linear curves statistically, the tumor was categorized according to the curve with the larger coefficient of determination (R^2). In each case in which the pattern of growth fit either exponential or linear growth, tumor doubling time was estimated from each regression equation.

Biological Differences Between Skull Base and Non–Skull Base Meningiomas

To evaluate biological differences between skull base and non–skull base meningiomas, we subsequently analyzed 210 consecutive meningioma specimens, which were surgically obtained during the same period (1993–2005). All meningiomas were histologically defined as Grade I tumors based on the WHO 2007 classification. Atypical (Grade II) and anaplastic (Grade III) tumors were excluded. Magnetic resonance imaging studies used to determine tumor location and clinicopathological characteristics such as sex, age, and histological subtype were reviewed. The MIB-1 indices were also obtained for all 210 specimens as previously described.[13]

Statistical Analysis

Regression analysis and other types of statistical analysis such as the Fisher exact test and Mann-Whitney U-test for independence were performed using statistical

software (version 5.0, Statview, SAS Institute, Inc.) with a p value < 0.05 considered significant.

Results

Volumetric Comparison of Growth Rates and Patterns Between Skull Base and Non–Skull Base Meningiomas

Demographic data are summarized in Table 1. A total of 113 IDMs from 110 patients were included in this study; 2 patients had multiple tumors. There were 93 women and 17 men, and the mean age was 66.8 years (range 37–91 years). The mean follow-up period for sequential MR images was 46.9 months, ranging from 12 to 121 months. Table 2 shows the distribution of the cases based on location. Thirty-eight (34%) were located in the skull base and 75 (66%) were not.

Of the 113 IDMs, 42 tumors (37%) showed no growth during the follow-up period and 71 (63%) showed growth. Interestingly, when all IDMs were divided into skull base and non–skull base categories, only 15 (39.5%) of 38 skull base meningiomas showed growth, whereas 56 (74.7%) of 75 non–skull base meningiomas showed growth (Fig. 1; p = 0.0004, Fisher exact test). Of the 38 skull base IDMs, 22 (57.9%) did not grow, and 1 reduced in volume.

As shown in Table 3, of the 71 IDMs that showed growth, no statistically significant difference was noted between the skull base and non–skull base groups in terms of mean age, sex, follow-up period, or initial tumor volume. However, the annual relative growth rate (p = 0.009) and the percentage of growth (p = 0.002) were much lower in the skull base group than in the non–skull base group. Accordingly, with slower growth rate, the tumor doubling time (p = 0.008) was much higher in the skull base group.

To further exemplify the differential growth rate between the 2 groups, the case of a 67-year-old man with multiple meningiomas, who underwent follow-up for 25 months, is presented. The patient had 1 cavernous and 2 convexity meningiomas (Fig. 2). The doubling time for the skull base tumor was 261 months, whereas for the 2 convexity-located tumors, it was 162 and 116 months, with the latter showing growth of more than 15%.

We also analyzed the growth pattern of these tumors (Table 4). Unexpectedly, 60% of skull base IDMs showed an exponential pattern of growth, whereas 32% of non–skull base IDMs showed an exponential pattern. Only 14% of non–skull base tumors showed no trend in growth pattern. In Fig. 2 (dotted lines), we can see that the cavernous tumor fitted better to an exponential curve and the 2 convexity tumors fitted better to a linear pattern using regression analysis. However, it is important to note that the R^2 for the 3 tumors statistically fit both linear and exponential curves (Fig. 2B). But as described in the methodology, in situations like this, the tumor will be categorized based on the pattern with a larger R^2.

The number of patients who became symptomatic and underwent treatment during the follow-up period was also different between the 2 groups (Table 5). Only 1 (2.6%) of 38 patients with skull base IDMs underwent surgery, whereas 6 (8.0%) of 75 patients with non–skull base IDMs needed surgery or radiotherapy.

Biological Differences in Skull Base and Non–Skull Base Meningiomas

To clarify the biological meaning of the volumetric results, we went back to the surgical cases seen in the same period. A summary of demographic data for the 210 consecutive symptomatic meningiomas is shown in Table 6. The mean age was 57.2 years (range 16–90 years). The incidence of male sex (25.7%) seemed higher in this series than in that of the IDMs, but it is comparable to the previously reported incidence.[18] Histological subtypes were also verified and consisted of meningothelial (44.3%), transitional (21.0%), fibrous (19.0%), angiomatous (5.2%), psammomatous (5.2%), and other (5.2%) subtypes. There were 94 skull base and 116 non–skull base meningiomas. No statistical difference was noted according to the age or sex ratio. However, the mean MIB-1 index for skull base tumors was markedly low (2.09%) compared with that for non–skull base tumors (2.74%; p = 0.013; Table 6 and Fig. 3).

Because male sex is a well-known factor that affects the biological behavior of meningiomas in general, the difference between female and male sex was also analyzed. As expected, the highest mean MIB-1 index (3.16%) was seen in males with non–skull base tumors, and the lowest (1.82%) in females with skull base tumors. A statistically significant difference was observed between all male and all female cohorts (p = 0.045), as well as between male and female cohorts with skull base tumors (p = 0.021; Table 7).

Discussion

Several reports have been published regarding the

TABLE 1: Demographic data of 113 IDMs for volumetric analyses

Variable	All	Skull Base	Non–Skull Base
no. of cases (%)	113	38 (34)	75 (66)
mean age in yrs (range)	66.8 (37–91)	66.8 (40–84)	66.8 (37–91)
sex ratio (F:M)	93:17	29:9	64:8
mean follow-up period in mos (range)	46.9 (12–121)	40.3 (12–100)	50.3 (12–121)
mean initial tumor volume in cm^3 (range)	9.79 (0.32–86.62)	12.22 (0.56–86.62)	8.56 (0.32–74.69)
no. w/o growth (%)	42 (37)		
no. w/ growth (%)	71 (63)		

TABLE 2: Distribution of all IDM cases based on location

Location	No. of Cases
convexity	35
falx	17
petroclival	17
parasagittal	14
sphenoid wing	7
cavernous	6
intraventricular	4
planum sphenoidale	4
tentorium	4
olfactory	3
other	2

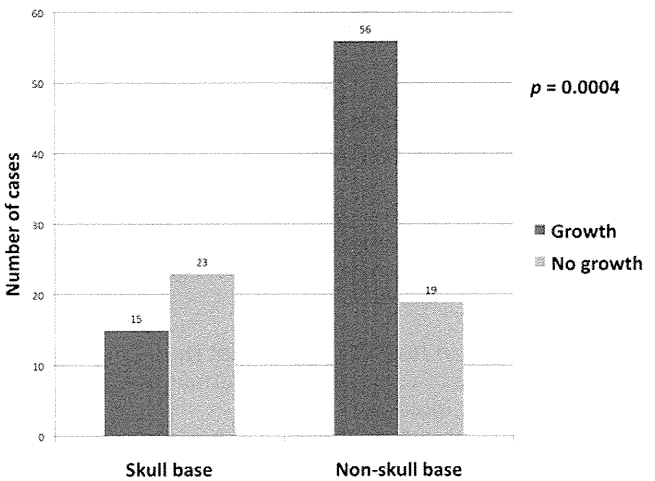

FIG. 1. Incidence of meningiomas showing growth and no growth in skull base and non–skull base tumors. Fifteen (39.5%) of 38 skull base tumors showed growth, whereas 56 (74.7%) of 75 non–skull base tumors showed growth (p = 0.0004, Fisher exact test).

natural history of IDMs using various means of growth measurement, some using linear (diameter)[4,9,16,21,23] and some using volumetric[6,14,15,24] methods. According to these studies, the natural history of IDMs can be summarized in 3 points. First, most IDMs (or at least a subset of IDMs) may not grow for a certain period of time. Second, for tumors that grow, the rate of growth seems slow. In our previous report, the mean tumor volume doubling time in growing IDMs was 93.6 months (7.8 years). Finally, hyperintensity on T2-weighted imaging is positively correlated with growth, whereas the presence of calcification is negatively correlated with tumor growth. As to the impact of tumor location on growth behavior, probably because of the small number of patients, this has yet to be reported. In this paper, we found that IDMs in the skull base tended not to grow when compared with those in non–skull base locations. Furthermore, even if these tumors grow, the rate of growth was significantly lower in terms of the percentage growth, annual growth rate, and rates of experiencing symptoms and undergoing treatment.

In this report, we also found that there was a statistically significant difference in the MIB-1 index, which is thought of as a biological marker of cell proliferation, between skull base and non–skull base meningiomas. This is in line with previous studies indicating the existence of biological differences between the two.[8,10,11,20] Kasuya et al.[8] reported that male sex, the absence of calcification on imaging, and non–skull base location are independent risk factors for a high MIB-1 index by logistic regression analysis among 342 consecutive surgical cases. More recently, McGovern et al.[11] made an important note that meningiomas with a non–skull base location are more likely to have a higher MIB-1 index and recur with a higher grade than those within the skull base. Sade et al.[20] found that the incidence of Grade II and III tumors is significantly higher outside the skull base (12.1%) than in the skull base (3.5%) from the records of 794 consecutive patients. Mahmood and colleagues[10] likewise noted that among their 319 patients, 25 had Grade II and III tumors, of which, 7 (28%) were located at the skull base and 18 (72%) were outside the skull base. In the latest study from

TABLE 3: Comparison between skull base and non–skull base lesions in 71 growing IDMs*

Variable	Skull Base (range)	Non–Skull Base (range)	p Value	Statistics Used
no. of cases	15	56		
mean age in yrs	69.5 (40–83)	66.6 (37–91)	0.320	M-W
sex ratio (F:M)	11:4	48:6	0.207	Fisher
mean follow-up period in mos	49.3 (20–100)	53.1 (12–121)	0.485	M-W
mean initial tumor volume in cm^3	14.71 (0.79–86.62)	8.11 (0.32–74.69)	0.163	M-W
absolute growth rate in cm^3/yr	1.20 (0.02–7.85)	1.15 (0.04–11.33)	0.662	M-W
relative growth rate %/yr	6.84 (2–24)	13.78 (2–74)	0.009†	M-W
% growth	25.56 (15.57–43.27)	94.83 (16.11–1519.67)	0.002†	M-W
mean tumor doubling time	160.8 (39–383)	111.5 (15–420)	0.008†	M-W

* M-W = Mann-Whitney.
† Statistically significant.

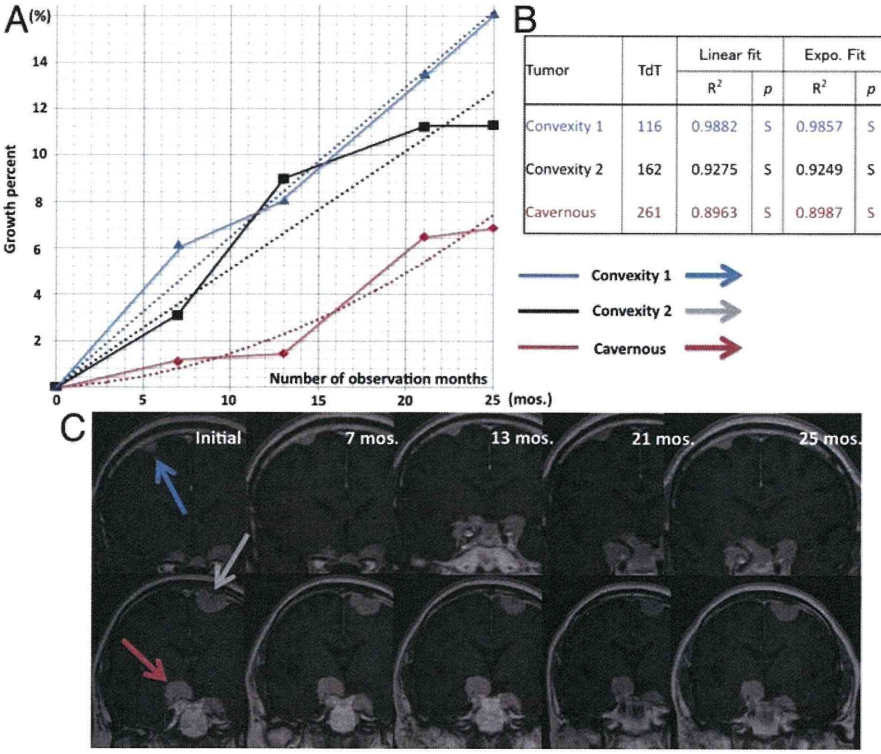

FIG. 2. Sequential volumetric data **(A)**, the data for growth rates and results of regression analyses **(B)**, and MR images **(C)** from a representative case of a 67-year-old man with multiple IDMs. Note that the percentage of growth of cavernous IDMs *(red line)* is smaller than those of convexity ones (*gray* and *blue lines*). Expo. = exponential; Judg. = judgment of growth pattern; p = p value; R^2 = coefficient of determination; S = statistically significant; TdT = tumor doubling time. Refer to the text for explanation of the dotted lines.

Kane et al.,[7] based on their statistical observation of 378 surgical cases, they reported that anatomical location is a risk factor for Grade II and III meningiomas.

All these reports, including ours, seem to suggest that non–skull base meningiomas have a more aggressive behavior. In 2003, we proposed that loss of 1p is significantly correlated with malignant progression of meningiomas by analyzing 72 tumors, including WHO Grade II and III tumors, with fluorescence in situ hybridization and loss of heterozygosity analyses.[13] This small study included 49 Grade I, 15 Grade II, and 8 Grade III tumors. Although the data were not shown in this paper, it was our impression that most Grade II and III tumors are found in a parasagittal (non–skull base) location. Therefore, we decided to categorize these tumors according to location, and we were able to obtain a statistically significant difference in the percentage of cells with 1p deletions (Table 8). We noted that skull base meningiomas harbored a significantly lower percentage of cells with 1p loss (20.31%) compared with non–skull base tumors (37.87%). This observation seems to further suggest that skull base tumors may indeed have fewer genetic aberrations and may have a less aggressive biological nature.

Regarding growth patterns, Nakasu et al.[15] and our group[6] reported that IDMs do not always grow exponentially and show various patterns of growth including a linear pattern. Based on the rule of proliferation kinetics, tumors with an exponential pattern of growth will maintain their cell-doubling time constant over time. In contrast, those with linear growth patterns will have a reduced cell-doubling time over time. In this study, 60% of skull base IDMs showed an exponential pattern of growth, whereas 33% of non–skull base IDMs showed an exponential pattern. However, these data must be cautiously interpreted because most of the tumors did fit both exponential and linear patterns statistically when regression analysis was performed. In fact, among the 63 tumors with either a linear or exponential growth pattern described in Table 4, only 1 tumor fit an exclusively linear pattern (data not shown). In other words, the data in Ta-

TABLE 4: Growth patterns of 71 growing IDMs

Pattern	No. of Cases (%)	
	Skull Base	Non–Skull Base
no trend	0 (0)	8 (14)
exponential	9 (60)	18 (32)
linear	6 (40)	30 (54)

TABLE 5: Summary of clinical courses of 113 IDMs

Course	No. of Cases (%)	
	Skull Base	Non–Skull Base
remained asymptomatic	37 (97.4)	69 (92.0)
underwent surgery	1 (2.6)	4 (5.3)
underwent radiotherapy	0	2 (2.7)

TABLE 6: Biological comparison between skull base and non–skull base symptomatic meningiomas

Variable	All	Skull Base	Non–Skull Base	p Value (statistic)*
no. of cases	210	94	116	
age in yrs				0.096 (unpaired t-test)
mean	57.2	55.5	58.6	
range	16–90			
sex ratio (F:M)	156:54	68:26	88:28	0.635 (Fisher)
MIB-1 index (%)				0.013 (unpaired t-test)†
mean	2.45	2.09	2.74	
range	0.1–11.1			

* The p values represent the differences between the skull base and non–skull base symptomatic meningiomas.
† Statistically significant.

ble 4 reflect the fact that we took the larger coefficient of determination (R^2) in each tumor. Therefore, we believe that it is still too early to conclude that skull base tumors are more likely to present with an exponential pattern of growth. Longer follow-up periods and more cases are still warranted.

We believe that our findings may contribute to the understanding of the natural history of IDMs. It may also impact the way we currently manage IDMs. Those with a skull base location can be observed with sequential follow-up MR images more safely and longer than those with non–skull base tumors, except when they are located at the medial sphenoidal region adjacent to the optic nerve. We may be able to recommend a longer interval of follow-up MR imaging in skull base IDMs than in non–skull base tumors after confirming that IDMs tend not to grow during the early phase of follow-up.

For IDMs that became symptomatic or for uncomplicated symptomatic meningiomas requiring intervention, the findings in this paper may also be useful. As has been reported before, non–skull base meningiomas are more amenable to total resection and have better recurrence-free survival rates,[11] whereas total resection of skull base meningiomas may be limited by adjacent critical structures including the brainstem and cranial nerves. Black and colleagues[1] reported a series of 100 patients with skull base meningiomas who were treated with a combination of aggressive surgery and conformal radiation therapy. The authors found that this approach yielded an acceptable functional status in 99% of patients. McGovern et al.[11] also reported that adjuvant radiation therapy for skull base meningiomas improved the recurrence-free survival rate of subtotally resected skull base tumors to levels similar to those that were completely resected. Consistent with their suggestion, and taking into consideration the findings in this paper that skull base meningiomas have less aggressive behavior, it seems that maximal surgical reduction limited by the preservation of patient performance status, and the addition of postoperative radiotherapy or radiosurgery,[2,5] intensity-modulated radiotherapy,[12,19] and proton therapy,[22] may be an acceptable option for these patients.

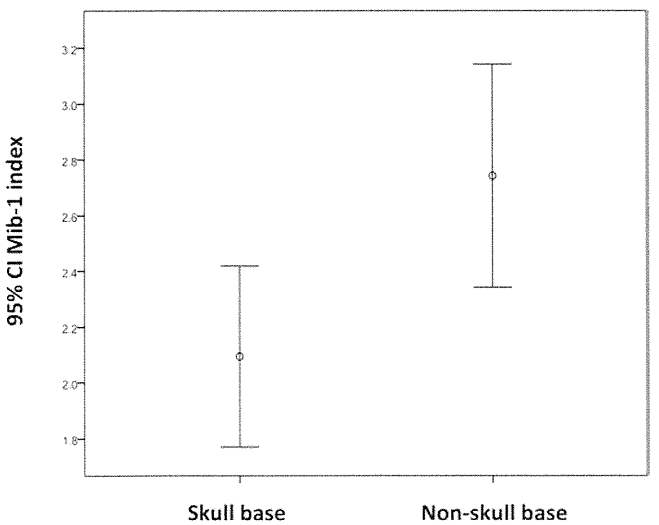

FIG. 3. Graph showing the MIB-1 index in surgical specimens from the skull base and non–skull base groups. The mean MIB-1 index for skull base tumors was markedly low (2.09%) compared with that for non–skull base tumors (2.74%; p = 0.013). *Circles* show the mean MIB-1 index, and *bars* show the 95% CI.

Conclusions

A sequential volumetric analysis of 113 IDMs revealed that skull base IDMs tended not to grow compared with non–skull base IDMs. Even when the skull base IDMs grow, the rate of growth is significantly lower than that for non–skull base tumors. Furthermore, a biological comparison of skull base and non–skull base sur-

TABLE 7: Relation of MIB-1 index to location and sex

Variable	Male	Female	p Value (unpaired t-test)
no. of cases	54	156	
mean age in yrs	59.59	56.42	0.13
mean MIB-1 (%)			
all	2.99	2.27	0.045*
skull base	2.82	1.82	0.021*
non–skull base	3.16	2.61	0.249

* Statistically significant.

TABLE 8: Loss of 1p by genetic analysis and location

Location	No.	Mean % Cells w/ 1p Loss*
Skull base	17	20.31
Non–skull base	55	37.87

* p = 0.019 (Mann-Whitney).

gically treated meningiomas in 210 consecutive patients showed that the mean MIB-1 index was significantly lower in skull base tumors. These findings may impact our understanding of the natural history of IDMs, as well as the strategies for management and treatment, not only of IDMs, but also of symptomatic meningiomas.

Disclosure

This work was supported in part by Grants-in-Aid No. 22103508 for Scientific Research of Computational Anatomy from the Ministry of Education, Science, Sports and Culture, Japan, to Naoya Hashimoto, M.D., Ph.D.

Author contributions to the study and manuscript preparation include the following. Conception and design: Hashimoto, Yoshimine. Acquisition of data: Hashimoto, Rabo, Okita, Kagawa, Fujimoto, Morii. Analysis and interpretation of data: Hashimoto, Kinoshita, Morii. Drafting the article: Hashimoto, Rabo. Critically revising the article: all authors. Reviewed submitted version of manuscript: all authors. Approved the final version of the manuscript on behalf of all authors: Hashimoto. Statistical analysis: Hashimoto, Rabo. Administrative/technical/material support: Kagawa. Study supervision: Yoshimine.

Acknowledgment

The authors would also like to thank Ms. Mariko Kakinoki for her secretarial assistance.

References

1. Black PM, Villavicencio AT, Rhouddou C, Loeffler JS: Aggressive surgery and focal radiation in the management of meningiomas of the skull base: preservation of function with maintenance of local control. **Acta Neurochir (Wien) 143:** 555–562, 2001
2. Elia AE, Shih HA, Loeffler JS: Stereotactic radiation treatment for benign meningiomas. **Neurosurg Focus 23(4):**E5, 2007
3. Firsching RP, Fischer A, Peters R, Thun F, Klug N: Growth rate of incidental meningiomas. **J Neurosurg 73:**545–547, 1990
4. Go RS, Taylor BV, Kimmel DW: The natural history of asymptomatic meningiomas in Olmsted County, Minnesota. **Neurology 51:**1718–1720, 1998
5. Han JH, Kim DG, Chung HT, Park CK, Paek SH, Kim CY, et al: Gamma knife radiosurgery for skull base meningiomas: long-term radiologic and clinical outcome. **Int J Radiat Oncol Biol Phys 72:**1324–1332, 2008
6. Hashiba T, Hashimoto N, Izumoto S, Suzuki T, Kagawa N, Maruno M, et al: Serial volumetric assessment of the natural history and growth pattern of incidentally discovered meningiomas. Clinical article. **J Neurosurg 110:**675–684, 2009
7. Kane AJ, Sughrue ME, Rutkowski MJ, Shangari G, Fang S, McDermott MW, et al: Anatomic location is a risk factor for atypical and malignant meningiomas. **Cancer 117:**1272–1278, 2011
8. Kasuya H, Kubo O, Tanaka M, Amano K, Kato K, Hori T: Clinical and radiological features related to the growth potential of meningioma. **Neurosurg Rev 29:**293–297, 2006
9. Kuratsu J, Kochi M, Ushio Y: Incidence and clinical features of asymptomatic meningiomas. **J Neurosurg 92:**766–770, 2000
10. Mahmood A, Caccamo DV, Tomecek FJ, Malik GM: Atypical and malignant meningiomas: a clinicopathological review. **Neurosurgery 33:**955–963, 1993
11. McGovern SL, Aldape KD, Munsell MF, Mahajan A, DeMonte F, Woo SY: A comparison of World Health Organization tumor grades at recurrence in patients with non-skull base and skull base meningiomas. Clinical article. **J Neurosurg 112:** 925–933, 2010
12. Milker-Zabel S, Zabel-du Bois A, Huber P, Schlegel W, Debus J: Intensity-modulated radiotherapy for complex-shaped meningioma of the skull base: long-term experience of a single institution. **Int J Radiat Oncol Biol Phys 68:**858–863, 2007
13. Murakami M, Hashimoto N, Takahashi Y, Hosokawa Y, Inazawa J, Mineura K: A consistent region of deletion on 1p36 in meningiomas: identification and relation to malignant progression. **Cancer Genet Cytogenet 140:**99–106, 2003
14. Nakamura M, Roser F, Michel J, Jacobs C, Samii M: The natural history of incidental meningiomas. **Neurosurgery 53:** 62–71, 2003
15. Nakasu S, Fukami T, Nakajima M, Watanabe K, Ichikawa M, Matsuda M: Growth pattern changes of meningiomas: long-term analysis. **Neurosurgery 56:**946–955, 2005
16. Olivero WC, Lister JR, Elwood PW: The natural history and growth rate of asymptomatic meningiomas: a review of 60 patients. **J Neurosurg 83:**222–224, 1995
17. Onizuka M, Suyama K, Shibayama A, Hiura T, Horie N, Miyazaki H: Asymptomatic brain tumor detected at brain checkup. **Neurol Med Chir (Tokyo) 41:**431–435, 2001
18. Perry A, Louis DN, Scheithauer BW, Budka H, von Deimling A: Meningiomas, in Louis DN, Ohgaki H, Wiestler OD, et al (eds): **WHO Classification of Tumours of the Central Nervous System, ed 4.** Lyon: IARC press, 2007, pp 164–172
19. Pirzkall A, Debus J, Haering P, Rhein B, Grosser KH, Höss A, et al: Intensity modulated radiotherapy (IMRT) for recurrent, residual, or untreated skull-base meningiomas: preliminary clinical experience. **Int J Radiat Oncol Biol Phys 55:**362–372, 2003
20. Sade B, Chahlavi A, Krishnaney A, Nagel S, Choi E, Lee JH: World Health Organization Grades II and III meningiomas are rare in the cranial base and spine. **Neurosurgery 61:**1194–1198, 2007
21. Sughrue ME, Rutkowski MJ, Aranda D, Barani IJ, McDermott MW, Parsa AT: Treatment decision making based on the published natural history and growth rate of small meningiomas. A review and meta-analysis. **J Neurosurg 113:**1036–1042, 2010
22. Vernimmen FJ, Harris JK, Wilson JA, Melvill R, Smit BJ, Slabbert JP: Stereotactic proton beam therapy of skull base meningiomas. **Int J Radiat Oncol Biol Phys 49:**99–105, 2001
23. Yano S, Kuratsu J: Indications for surgery in patients with asymptomatic meningiomas based on an extensive experience. **J Neurosurg 105:**538–543, 2006
24. Yoneoka Y, Fujii Y, Tanaka R: Growth of incidental meningiomas. **Acta Neurochir (Wien) 142:**507–511, 2000

Manuscript submitted June 9, 2011.
Accepted November 2, 2011.
Please include this information when citing this paper: published online December 16, 2011; DOI: 10.3171/2011.11.JNS11999.

Address correspondence to: Naoya Hashimoto, M.D., Ph.D., Department of Neurosurgery, Osaka University Graduate School of Medicine, Yamada-oka 2-2, Suita City, Osaka 565-0871, Japan. email: hashimotonaoya@me.com.

Novel Animal Glioma Models that Separately Exhibit Two Different Invasive and Angiogenic Phenotypes of Human Glioblastomas

AQ: au

Satoshi Inoue[1], Tomotsugu Ichikawa[1], Kazuhiko Kurozumi[1], Tomoko Maruo[1], Manabu Onishi[1], Koichi Yoshida[1], Kentaro Fujii[1], Hirokazu Kambara[1], E. Antonio Chiocca[2], Isao Date[1]

Key words
- Angiogenesis
- Animal brain tumor model
- Glioma
- Invasion

Abbreviations and Acronyms
BBB: Blood-brain barrier
DNA: Complementary DNA
CNS: Central nervous system
DAB: Diaminobenzidine
DAPI: 4′,6-diamino-2-phenylindole
DMEM: Dulbecco's modified Eagle's medium
FBS: Fetal bovine serum
GAPDH: ••
GFP: Green fluorescent protein
HIF-1: Hypoxia-inducible factor-1
MAP: ••
MMP-2: Matrix metalloproteinase-2
MMP-9: Matrix metalloproteinase-9
MRI: Magnetic resonance imaging
PBS: Phosphate-buffered saline
PCR: Polymerase chain reaction
PDGF: Platelet-derived growth factor
RECA-1: ••
SPARC: Secreted protein acidic and rich in cysteine
VEGF: Vascular endothelial growth factor

From the [1]Department of Neurological Surgery, Okayama University Graduate School of Medicine, Dentistry and Pharmaceutical Sciences, Okayama, Japan; and [2]Dardinger Laboratory for Neuro-oncology and Neurosciences, Department of Neurological Surgery, James Comprehensive Cancer Center and The Ohio State University Medical Center, Columbus, Ohio, USA

To whom correspondence should be addressed: Tomotsugu Ichikawa, M.D., Ph.D. [E-mail: tomoichi@cc.okayama-u.ac.jp]

Citation: World Neurosurg. (2011) xx, x:xxx.
DOI: 10.1016/j.wneu.2011.09.005
Journal homepage: www.WORLDNEUROSURGERY.org
*Available online: **www.sciencedirect.com***

OBJECTIVE: Invasive behaviors of malignant gliomas are fundamental traits and major reasons for treatment failure. Delineation of invasive growth is important in establishing treatment for gliomas and experimental neuro-oncology could benefit from an invasive glioma model. In this study, we established two new cell line-based animal models of invasive glioma.

METHODS: Two cell lines, J3T-1 and J3T-2, were derived from the same parental canine glioma cell line, J3T. These cells were inoculated to establish brain tumors in athymic mice and rats. Pathologic samples of these animal gliomas were examined to analyze invasive patterns in relation to angiogenesis, and were compared with human glioblastoma samples. The molecular profiles of these cell lines were also shown.

RESULTS: Histologically, J3T-1 and J3T-2 tumors exhibited different invasive patterns. J3T-1 cells clustered around newly developed vessels at tumor borders, whereas J3T-2 cells showed diffuse single cell infiltration into surrounding normal parenchyma. In human malignant glioma samples, both types of invasion were observed concomitantly. Molecular profiles of these cell lines were analyzed by immunocytochemistry and with quantitative reverse transcription polymerase chain reaction. Vascular endothelial growth factor, matrix metalloproteinase-9, hypoxia-inducible factor-1, and platelet-derived growth factor were overexpressed in J3T-1 cells rather than in J3T-2 cells, whereas integrin $\alpha v\beta 3$, matrix metalloproteinase-2, nestin, and secreted protein acidic and rich in cysteine were overexpressed in J3T-2 cells rather than in J3T-1 cells.

CONCLUSIONS: These animal models histologically recapitulated two invasive and angiogenic phenotypes, namely angiogenesis-dependent and angiogenesis-independent invasion, also observed in human glioblastoma. These cell lines provided a reproducible in vitro and in vivo system to analyze the mechanisms of invasion and angiogenesis in glioma progression.

INTRODUCTION

Malignant glioma is the most common primary brain tumor in adults. It is characterized by rapid expansion, invasion of adjacent central nervous system (CNS) tissues, and aberrant vascularization (32, 49). Despite recent advances in treatment with surgery, radiation, and chemotherapy, patients with glioblastoma have less than 2-year median survival after diagnosis, and only 16.0% survive beyond 3 years (43).

Invasion by tumor cells into surrounding brain tissue is a major problem in managing malignant glioma. It is the reason why resection is not curative, it leads to relapse and death, and it has been investigated extensively (18). Almost 70 years ago, in a series of 120 untreated gliomas, Scherer (41) showed an infiltrative growth pattern that was associated with distinct anatomic structures—tumor cells followed myelinated axons and the basement membranes of blood vessels (18).

Several factors make it difficult to analyze invasion. One is the lack of glioma-specific staining for pathologic analysis. Exact localization of invading glioma cells in seemingly normal brain parenchyma is crucial for the precise evaluation of invasion patterns. Recently, MAP2e, a splice variant of MAP-2, has been reported as a candidate glioma-specific antigen. Most cells in CNS tumors, particularly oligodendrogliomas and glioblastomas, are intensely stained and permit visualization of invasive glioma

cells (44). Another reason for difficulty in analyzing invasion is that there are few, if any, transplantable animal models that show an invasive growth pattern. Typically, transplantable tumors in mice or rats form solid nodules at the injection site, which compress rather than invade the surrounding brain (49).

Delineation of invasive growth is very important in establishing treatment for gliomas and experimental neuro-oncology could benefit from invasive glioma models that exhibit different histologic patterns (1, 8, 20).

In the present study, we established two new cell line-based animal models of invasive glioma that reflect the invasive phenotype of malignant gliomas in humans. Pathologic samples of these animal gliomas were examined to analyze invasive patterns in relation to angiogenesis and were compared with human glioblastoma samples. The molecular profiles of these animal models were also shown.

MATERIALS AND METHODS

Cell Preparation

J3T canine glioma cells were generous gift from Dr. Michael E. Berens (Translation Genomics Research Institute, Phoenix, Arizona, USA) (5). Two cell lines (J3T-1 and J3T-2) were developed from a parental J3T cell line, as previously described (22). Briefly, J3T cells (5×10^6) were implanted subcutaneously into the flanks of two athymic mice (NCr/Sed, nu/nu; 20 g). After 6 weeks, two tumors were established in two animals. Tumors were harvested in a sterile fashion, minced with a scalpel in 1-mm^3 cubes, treated for 1 hour with 1 mg/mL collagenase/dispase (Roche, Basel, Switzerland) and subsequently cultured in Dulbecco's modified Eagle's medium (DMEM) supplemented with 10% fetal bovine serum (FBS), 100 units of penicillin, and 0.1 mg/mL of streptomycin. J3T-1 and J3T-2 cell lines were each derived from single subcutaneous tumors.

For enhanced visualization of J3T-1 and J3T-2 cells, we established cell lines that stably expressed green fluorescent protein (GFP). J3T-1 and J3T-2 cells were transfected with the pAcGFP1-C1 plasmid (Clontech Laboratories Inc., Mountain View, California, USA), which encoded GFP using TransIT-LT1 reagent (Takara Bio Inc., Otsu, Shiga, Japan) to make J3T-1G and J3T-2G. Cells were cultured in DMEM supplemented with 10% FBS, 100 units of penicillin, and 0.1 mg/mL of streptomycin.

Animal Glioma Xenograft Model

All experimental animals were housed and handled in accordance with the Okayama University Animal Research Committee guidelines. Before implantation, 85% to 90% of confluent J3T-1, J3T-2, J3T-1G, and J3T-2G cells were trypsinized, rinsed with DMEM + 10% FBS, and centrifuged at 800 rpm for 5 minutes. The resulting pellet was resuspended in phosphate-buffered saline (PBS) and concentration was adjusted to 1×10^5 cells/μL of PBS. Athymic rats (F344/N-nu/nu CLEA Japan, Inc., Tokyo, Japan) and mice (balb/c-nu/nu; CLEA Japan, Inc.) were used for the animal experiments. To establish brain tumor models, animals were anesthetized with intraperitoneal nembutal (30 mg/kg) and placed in a stereotactic apparatus (Narishige, Tokyo, Japan). Tumor cells (athymic rat: 5×10^5 cells/5 μL, athymic mouse: 2×10^5 cells/2 μL) were slowly injected into the basal ganglia of the right cerebral hemisphere (athymic rat: 4 mm lateral and 1 mm anterior to the bregma at a depth of 4 mm; athymic mouse: 3 mm lateral and 1 mm anterior to the bregma at a depth of 3 mm) using a Hamilton syringe (Hamilton, Reno, Nevada, USA) according to previously published procedures (22, 27). For histologic examination, athymic rats (J3T-1: $n = 5$, J3T-2: $n = 5$) were sacrificed 4 to 5 weeks after tumor inoculation and fixed in vivo by transcardiacal perfusion with 4% paraformaldehyde. Their brains were then removed and stored in 4% paraformaldehyde. To analyze survival time, we monitored xenograft models of J3T-1 ($n = 9$) and J3T-2 ($n = 8$) in athymic mice.

Immunofluorescence Analysis of Animal Brain Tumor Model

Animal brains were sliced into 16-μm sections for pathologic examination. Fluorescence microscopy was used to visualize implanted glioma cells. Snap-frozen tissue samples were embedded in optimal cutting temperature compound for cryosectioning and sliced into 16-μm sections for indirect immunofluorescence. Slides were incubated with 10% horse serum in PBS at room temperature for 60 minutes and then incubated overnight at 4°C with anti-RECA-1 antibody (1:20) (Abcam, Massachusetts, USA) diluted in PBS with 1% horse serum. After three washes with PBS, slides were incubated with anti-mouse IgG Cy3-conjugated antibody (Jackson ImmunoResearch Laboratories, Inc., West Grove, Pennsylvania, USA) and 4′,6-diamino-2-phenylindole (DAPI; 1:500) (Invitrogen, Tokyo, Japan) in PBS for 60 minutes. After three washes, coverslips were mounted on the slides using Gel/Mount (Biomeda, California, USA) and sections were examined using a fluorescence microscope equipped with triple fluorescent filter sets and a CCD camera connected to a computer.

Microvessel number and diameter were measured in 4-week-old brain tumors to assess angiogenic activity in these models (J3T-1, $n = 3$; J3T-2, $n = 3$). In both J3T-1 and J3T-2 xenograft models, five digital images were obtained (×200, 0.15 mm^2) from areas at the tumor borders and in the contralateral normal basal ganglia. Image J software (http://rsb.info.nih.gov/ij) was used to measure the number and diameter of vessels in these images. Statistical significance of vessel number and diameter was examined using the Mann-Whitney U test. P value less than 0.05 was considered to be statistically significant. Statistical analysis was performed using StatView statistical software (version 5.0; SAS Institute Inc., North Carolina, USA).

Magnetic Resonance Imaging in Animal Models

Animal brain tumors were analyzed using T_1- and T_2-weighted magnetic resonance imaging (MRI) 5 weeks after tumor inoculation (J3T-1, $n = 4$; J3T-2, $n = 4$). Animals were anesthetized with nembutal (30 mg/kg) and placed in a quadrature transmit/receive head coil (diameter, 28 cm). Coronal T_1-weighted images (repetition time, 400 ms; echo time, 11 ms; 2-mm thickness/0.2-mm gap; field of view, 12 × 12 cm; matrix, 256 × 256; 2 excitations) and T_2-weighted images (repetition time, 3000 m; echo time, 102 ms, 2-mm thickness/0.2-mm gap; field of view, 12 × 12 cm; matrix 256 × 256; 2 excitations) were obtained with a 1.5-tesla superconducting magnet MRI device (Signa Advantage version 5.4, General Electric, Milwaukee, Wisconsin, USA). Furthermore, coronal T_1-weighted im-

ages were obtained after an intravenous injection of gadolinium-diethylenetriaminepenta acetic acid (1.0 mL/kg) using the same MRI device.

Immunocytochemistry of Cultured Cell

J3T-1 and J3T-2 tumor cells were plated onto coverslips and cultured for 24 hours. These cells were washed three times with PBS and fixed with 4% paraformaldehyde for 10 minutes. Nonspecific binding was blocked by 10% horse serum in PBS for 1 hour at room temperature. Subsequently, cells were incubated 90 minutes at room temperature with anti-vascular endothelial growth factor (VEGF) antibody (1:20) (R&D systems, Minnesota, USA) and anti-integrin $\alpha v\beta 3$ antibody (1:100) (Millipore, Massachsetts, USA). Negative controls were treated similarly (time and temperature) with omission of the primary antibody. After washing, cells were incubated at room temperature with anti-mouse IgG Cy3-conjugated antibody (Jackson ImmunoResearch Laboratories, Inc., West Grove, Pennsylvania, USA) and DAPI (1:500) (Invitrogen) in PBS for 60 minutes. After three washes, coverslips were mounted on the slides using Gel/Mount (Biomeda). Fluorescent microscope equipped with triple fluorescent filter sets and a CCD camera connected to a computer was used to visualize fluorescence and to take pictures.

Quantitative Reverse Transcription Polymerase Chain Reaction Analysis of Cultured Cell

Total RNA was isolated from cultured J3T-1 and J3T-2 cells using RNeasy Mini Kit (QIAGEN, Valencia, California, USA) and was reverse transcribed with oligo dT primers using SuperScript III First-Strand Synthesis System for reverse transcription-polymerase chain reaction (PCR; Invitrogen, Carlsbad, California, USA) according to manufacturer's instructions. Primers specific for each gene target were designed using Primer Express Software (Applied Biosystems, Foster City, California, USA) and synthesized by Invitrogen. The resulting complementary DNA (cDNA) was amplified by PCR with gene-specific primers using 7300 Real Time PCR system (Applied Biosystems) and QuantiTect SYBR Green PCR Kit (QIAGEN). A log-linear relationship between amplification curve and quantity of cDNA in the range of 1 to 1000 copies were observed.

Quantification was done by Comparative Ct method using 7300 Real Time PCR System with Sequence Detection Software version 1.4 (Applied Biosystems). The cDNA amount in each sample was normalized to the crossing point of the housekeeping gene GAPDH. Thermal cycling parameters were as follows: denaturation at 95 °C for 10 minutes followed by 40 cycles at 95 °C for 15 seconds and 60 °C for 1 minute. Relative messenger RNA fold up-regulation in J3T-2 cells for each gene was calculated using the respective crossing points applied in the following formula: $F = 2^{(AH-AG)-(BH-BG)}$ where F = fold difference, A = J3T-2 cells, B = J3T-1 cells, H = housekeeping (GAPDH), and G = gene of interest.

Histopathologic Examination of Human Surgical Specimens

From April 2004 to March 2005, five consecutive samples of human glioblastoma were surgically removed en bloc, including surrounding normal brain parenchyma (Okayama University Hospital).

Glioma specimens were diagnosed and graded according to the World Health Organization classification of tumors of CNS by a neuropathologist. No patient received radiotherapy or chemotherapy before surgery.

Formalin-fixed and paraffin-embedded surgical specimens were sliced into 4-μm sections and mounted on microscopy slides (Thermo Fisher Scientific, Massachusetts, USA) for histopathologic examination. After deparaffinization in xylene and rehydration in decreasing concentrations of ethanol, sections were incubated in 0.3% hydrogen peroxide (30 minutes) and treated with an autoclave for 10 minutes at 121°C in distilled water. After three washes in PBS, sections were incubated at room temperature with anti-MAP2e monoclonal antibody (1:20 mouse IgG_1; gift from Bridget Shafit-Zagardo, Albert Einstein College of Medicine, Bronx, New York, USA) diluted in a solution of PBS and 5% skim milk (60 minutes). After incubation, sections were rinsed with PBS and incubated with secondary antibody against mouse IgG, which was applied using the DakoCytomation Envision+ System-HRP kit according to manufacturer's protocol (DakoCytomation, Carpinteria, California, USA), and diaminobenzidine (DAB). After three washes in PBS, sections were incubated overnight at 4°C with anti-vWf polyclonal antibody (1:300 rabbit, A0082, DakoCytomation). After incubation, sections were rinsed with PBS and incubated with secondary antibody against rabbit IgG with the DakoCytomation Envision+ System-HRP kit. Deep purple staining was achieved with DAB-nickel (0.05 M Tris-buffered saline containing 0.03% DAB and 0.06% nickel ammonium sulfate). After three washes, coverslips were mounted on the slides, and sections were examined with a microscope equipped with a CCD camera connected to a computer.

The degree of angiogenesis at the tumor borders, degree of perivascular MAP2e-positive cell cuffing, and density of single tumor cell infiltration in the cerebral cortex overlaying the tumor mass were determined. The degree of angiogenesis at the tumor borders was graded on a scale of 0 to 3+ as follows: 0, no detectable angiogenic activity; 1+, trace of dilated vessels; 2+, moderate number of dilated vessels; and 3+, high number of dilated vessels. Degree of perivascular MAP2e-positive cell cuffing was graded on a scale of 0 to 3+ as follows: 0, no detectable cuffing; 1+, patchy cuffing; 2+, near-circumferential thin cuffing; and 3+, circumferential thick cuffing. The density of single tumor cell infiltration in the cerebral cortex was graded on a scale of 0 to 3+ as follows: 0, no detectable tumor cells; 1+, sparse tumor cells at a density of less than 5 per high-power field; 2+, moderate tumor cells at a density of less than 20 per high-power field; and 3+, dense tumor cells at a density of >20 per high-power field. This classification was made by two neurosurgeons (S.I., T.M.) without prior knowledge of clinical or radiologic data of patients.

RESULTS

Two J3T Subclones Showed Different Invasive and Angiogenic Phenotypes in Animal Brains

Two subclones of the J3T canine glioma cell line, J3T-1 and J3T-2, were implanted in rat and mouse brains. Histologically, J3T-1 cells and J3T-2 tumors exhibited different morphologies (**Figure 1A–D**). When tested in athymic mice, similar histologic patterns

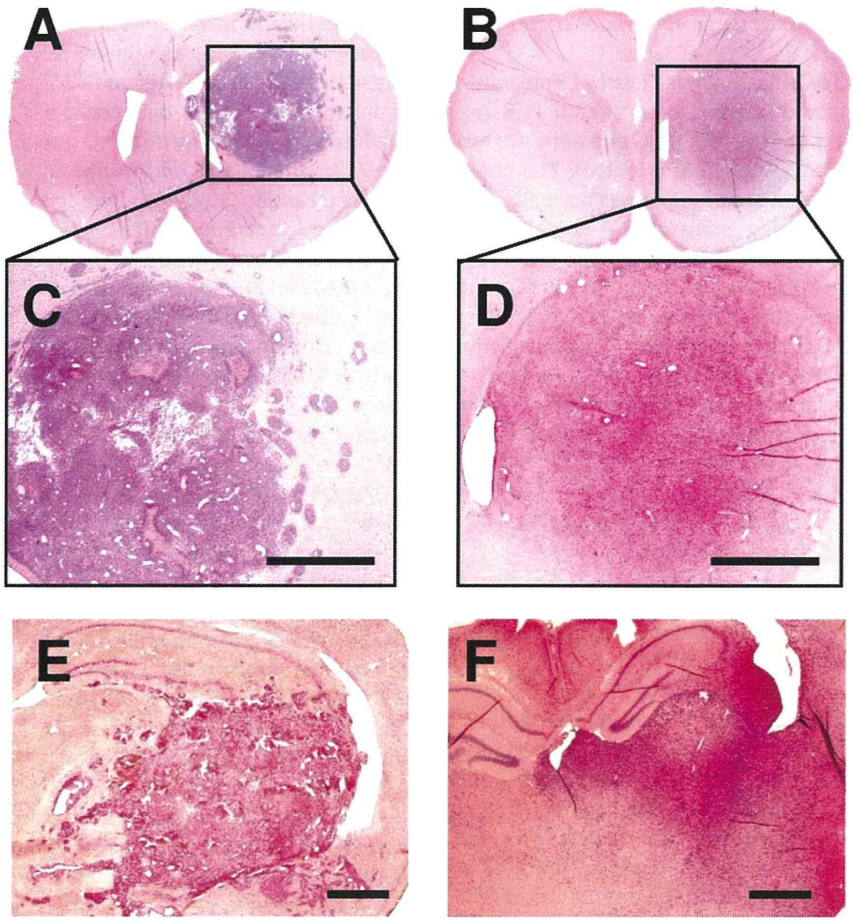

Figure 1. Macroscopic appearance of two distinct phenotypes of invasion in animals harboring J3T-1 and J3T-2 brain tumors. J3T-1 brain tumor established in athymic rat (**A, C**) and mouse (**E**) brains. J3T-1 cells formed well-demarcated and highly angiogenic tumors in the rat brain. Multiple small satellite tumors are also seen at tumor borders. J3T-2 brain tumor established in athymic rat (**B, D**) and athymic mouse (**F**) brains. J3T-2 cells gradually dispersed from the tumor center to the surrounding normal brain tissue. All sections were stained with hematoxylin-eosin. Scale bar = 1 mm.

were observed (**Figure 1E, F**). J3T-1 cells formed well-demarcated and highly angiogenic tumors in rat brains. At the center of the tumor, regions of high angiogenic activity with large number of dilated vessels were present. Furthermore, necrotic foci and pseudopalisading tumor cells were also seen. In normal parenchyma adjacent to the main tumor mass, multiple satellite tumor cells were seen with dilated blood vessels in F2 them (**Figure 2A**). In contrast, J3T-2 cells formed poorly demarcated tumors. Tumor cells gradually dispersed from the tumor center to the normal brain parenchyma with a gradient of cell density. Minimal angiogenesis was seen with a small number of slightly dilated vessels at the tumor center (**Figure 2B**). No dilated blood vessels or cluster of tumor cells were visible in areas distant from the tumor.

To facilitate tumor cell identification, J3T-1 and J3T-2 cells were transfected with the gene for GFP. In the J3T-1G model, cluster formation of tumor cells around dilated RECA-1-positive vessels was clearly shown by immunohistochemical staining (**Figure 3A**). No single cell infiltration was seen in the healthy brain. In the J3T-2G model, fluorescent microscopy clearly distinguished spindle-shaped tumor cells from normal glia or neuronal cells. Single cell infiltration independent of vasculature was seen in healthy brain tissue distant from the tumor center (**Figure 3B, C**). In the corpus callosum, stretched spindle cells turned in the direction of neuronal fibers and were distributed along them (**Figure 3D**). Spindle-shaped cells were also found dispersed along cortical axons.

Blood Vessel Morphology Differs Between J3T-1 and J3T-2 Tumors

To analyze the angiogenic activity in the invasive front of J3T-1 and J3T-2 brain tumors, brain sections were stained with RECA-1 and DAPI (**Figure 4**). In J3T-1 brain F4 tumors, large and dilated vessels, which were recognized as neovascular vessels, were located at the tumor borders. On the contrary, in J3T-2 tumors, no dilated vessels were seen at the tumor borders. In J3T-1 and J3T-2 tumors, the number of vessels at the tumor borders did not increase compared with that in contralateral healthy brain tissue. In contrast, the diameter of vessels in J3T-1 tumors, but not in J3T-2 tumors, was significantly increased compared with that in contralateral healthy brain tissue (J3T-1 vs. J3T-2: 1.62 ± 0.36-fold vs. 0.95 ± 0.14-fold, respectively; $P < 0.05$).

MRI of Rats With J3T-1 and J3T-2 Tumors Showed Different Characteristics

MRI of rats with J3T-1 and J3T-2 tumors was performed 5 weeks after tumor inoculation. Gadolinium-diethylenetriaminepenta acetic acid-enhanced T_1-weighted images of rats with J3T-1 tumors showed an enhancing mass lesion at the right basal ganglia. On T_2-weighted images, a wider area of high signal intensity was seen beyond the enhancing mass (**Figure 5A, B**). Compared F5 with J3T-1 tumors, J2T-2 tumors exhibited a diffuse high signal intensity area in the right basal ganglia on T_2-weighted images. There was no area of enhancement in these tumors (**Figure 5C, D**).

Survival of Mice Harboring J3T-1 and J3T-2 Brain Tumors F3

The cell doubling time of J3T-1 tumors was 19.5 hours and that of J3T-2 tumors was 17.4 hours. All athymic rats and mice inoculated with J3T-1 and J3T-2 developed brain tumors and died of tumor progression. The mean survival time of mice harboring J3T-1 ($n = 9$) and J3T-2 ($n = 8$) brain tumors was 33 days and 48 days, respectively (**Figure 6**). F6

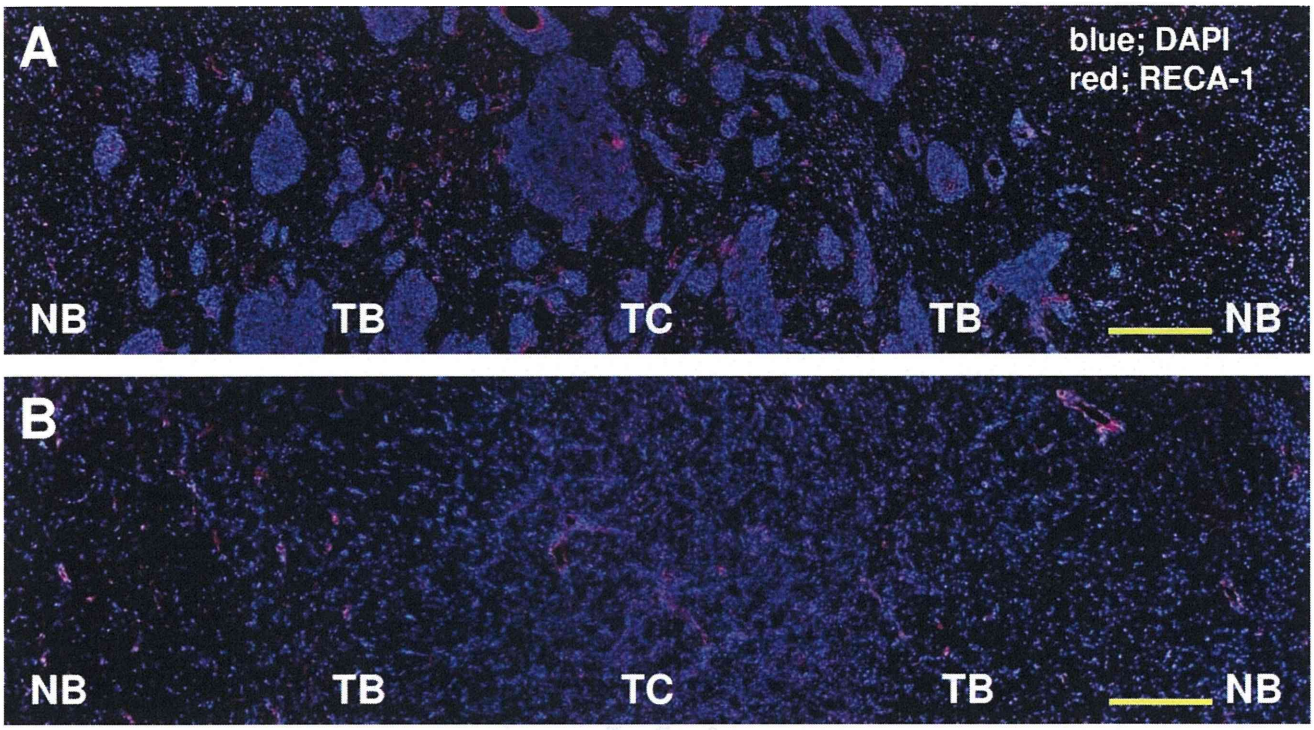

Figure 2. Fluorescent images of 4′,6-diamino-2-phenylindole (DAPI) nuclear staining (blue) and RECA-1 immunohistochemical staining (red). (**A**) J3T-1 brain tumor. Dilated vessels are present in the satellite tumors at tumor borders. (**B**) J3T-2 brain tumor. Dilated vessels at tumor borders are absent. Scale bar = 300 μm. TC, tumor center; TB, tumor border; NB, healthy brain tissue.

Two Phenotypes of Invasion Were Concurrently Seen in Human Glioblastomas

To analyze invasion patterns in relation to vasculature and to correlate these patterns with animal data, dual immunohistochemical staining with glioma-specific antibody (MAP2e) and endothelial-specific antibody (vWf) was performed in five human glioblastoma samples. The degree of angiogenesis at the tumor borders, the degree of perivascular MAP2e-positive cell cuffing, and the density of single tumor cell infiltration in the cerebral cortex overlaying the tumor mass were determined (**Table 1**). T1

All glioma cells in each sample were positive for MAP2e. The center of the tumor comprised an area of high-density tumor cells. Furthermore, necrosis and pseudopalisading glioma cells were seen in the core of the tumor (**Figure 7E**). Marked angiogenesis, which is characterized by thick endothelial proliferation, was seen in the center and at the tumor borders (**Figure 7B**). Furthermore, diffuse single cell infiltration from the tumor core to the surrounding healthy brain parenchyma (**Figure 7D, G**) was observed, thus rendering the border between the tumor and healthy brain tissue indistinct (**Figure 7A**). At the borders, clusters of MAP2e-positive cells were observed around dilated vessels in all cases (**Figure 7C, F**), despite some differences in the thickness of surrounding tumor cell layer, vessel density, and vessel diameter (**Table 1**). Cases 4 and 5 demonstrated fewer perivascular MAP2e-positive cells than cases 1 and 2. Infiltration by single cells distributed far beyond the area of cluster formation around new vessels. In distant areas, such as the cerebral cortex overlaying the tumor mass, scattered MAP2e-positive cells were also found in all animals; however, no dilated vessels or clusters of glioma cells around vessels were seen (**Figure 7D, G**). F7

Molecular Profile of J3T-1 and J3T-2 Cells by Immunocytochemistry

VEGF and integrin $\alpha v\beta 3$ are well-studied key molecules in angiogenesis and invasion, respectively. Immunocytochemistry against VEGF and integrin $\alpha v\beta 3$ in J3T-1 and J3T-2 cells were examined (**Figure 8**). VEGF was shown to be overexpressed in J3T-1 cells, whereas J3T-2 cells showed no expression (**Figure 8A, B**). On the other hand, J3T-2 cells overexpressed protein of integrin $\alpha v\beta 3$ compared with J3T-1 cells (**Figure 8C, D**).

Molecular Profile of J3T-1 and J3T-2 Cells by Quantitative Reverse Transcription PCR

A summary of quantitative reverse transcription PCR data is shown in **Figure 9**. Gene expression of matrix metalloproteinase-2 (MMP-2), nestin, and secreted protein acidic and rich in cysteine (SPARC) were higher in J3T-2 cells than in J3T-1 cells, whereas gene expression of matrix metalloproteinase-9 (MMP-9), hypoxia-inducible factor-1 (HIF-1), and platelet-derived growth factor (PDGF) were higher in J3T-1 cells than in J3T-2 cells. F9

DISCUSSION

Establishment of Novel Animal Glioma Models With Different Invasive Phenotypes

We have established two novel animal models with different invasive phenotypes and F8

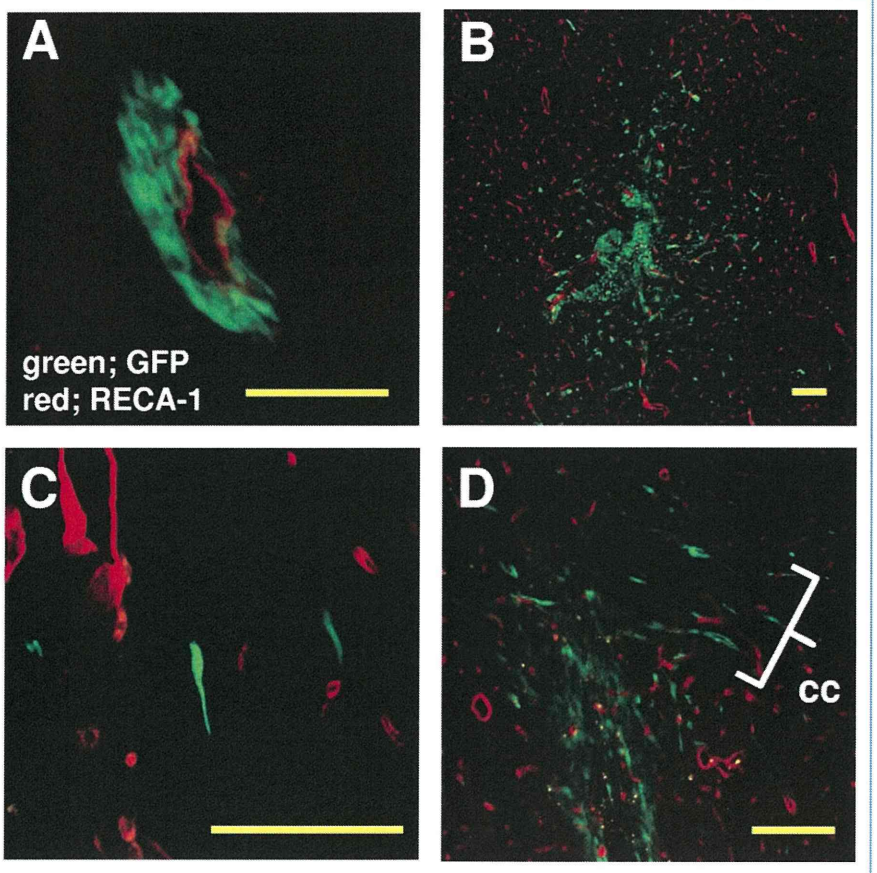

Figure 3. Immunofluorescent microscopy of tumor borders in brains harboring J3T-1G or J3T-2G tumors. J3T-1G cells expressing green fluorescent protein (GFP) coopting around dilated vessels (red). (**A**) J3T-2G single cells diffusely invaded healthy brain tissue (low magnification, **B** and high magnification, **C**) and turned toward the axons of the corpus callosum (**D**). Tumor cell (GFP, green), vascular stain (RECA-1, red), corpus callosum (cc). Scale bar = 100 μm.

have compared their pathologic features with that of human glioblastoma samples.

First, we established two cell subclones from the same parental cell line. These reproducibly established brain tumors with their inherent invasive phenotypes. It is possible that these differences in phenotype arose from differences in genotype. These genetic differences could have developed during culture in vitro due to genetic instability (35). J3T-1 cells formed densely packed, well-demarcated tumor mass with marked angiogenesis. In healthy parenchyma adjacent to the main tumor mass, clusters of tumor cells were seen with dilated blood vessels in them. In contrast, J3T-2 cells formed poorly demarcated tumors at the center. Diffuse infiltration by single cells was seen from the tumor center to the healthy brain parenchyma. These features, namely, perivascular cluster-forming invasion and single cell infiltration into normal parenchyma, were specific for each cell line and did not overlap with each other.

Second, we evaluated pathologic specimens of human glioblastoma and found that there were at least two invasive phenotypes: cluster formation around neovascular vessels, and single cell infiltration into healthy parenchyma.

On comparison of pathologic findings from experimental models and human glioblastoma samples, it was confirmed that each described animal glioma model represented the two phenotypes of human glioblastoma invasion.

The Two Invasive Phenotypes Are Angiogenesis Dependent and Angiogenesis Independent

Initially, we focused on tumor cell invasion, but found that invasion appears to be closely related to angiogenesis.

In animal models, J3T-1 was characterized by remarkable angiogenic activity and tumor cell cuffing around dilated vessels. In human samples, we found that tumor cell cuffing was only seen around dilated vessels with thickened epithelium in the marginal area, which is a characteristic of neovascular vessels (33). Therefore, we believe that tumor cells migrated along the abluminal surfaces of neovascular vessels and proliferated around them. Several investigators have reported similar findings in experimental models or in pathologic samples of human glioma (3, 11, 15). These reports showed glioma cell migration along vessels; however, these reports did not note the relationship between glioma cell invasion and angiogenesis. Holash et al. (23) reported vascular cooption of glioma cells and angiogenesis in the development of experimental glioma. Many molecules are known to be related to the development of angiogenesis. By comparative profiling of these cell lines, we have shown that VEGF, MMP-9, HIF-1, and PDGF were overexpressed in J3T-1 cells than in J3T-2 cells. VEGF is one of most important diffusible angiogenic factor secreted by coopting tumor cells (45). Several mechanisms have been implicated in hypoxia-driven VEGF production. Activation of VEGF messenger RNA transcription from DNA is mediated by binding of HIF-1. Autocrine or paracrine factors of the glioma microenvironment, PDGF, also contribute to the increased production of VEGF in gliomas (36). Raithatha et al. (38) reported that MMP-9 may regulate angiogenic remodeling. The endothelial cells stimulated by angiogenic factors then migrate and proliferate, resulting in neovascular formation (46). This paracrine loop leads to an extended foothold that allows tumor cells to migrate. As described previously, glioma cell cooption, perivascular migration, proliferation, and angiogenesis are closely related and progress concurrently (**Figure 10A**). Therefore, this invasive phenotype is exclusively angiogenesis dependent. The evidence that no single cell infiltration independent of vasculature was seen in the J3T-1 brain tumor model is a paradoxic proof of this phenomenon.

The infiltrative pattern of the J3T-2 xenograft model was different from that of J3T-1. J3T-2 cells migrated singly to healthy parenchyma, independent of vasculature, and showed a tendency to migrate along my-

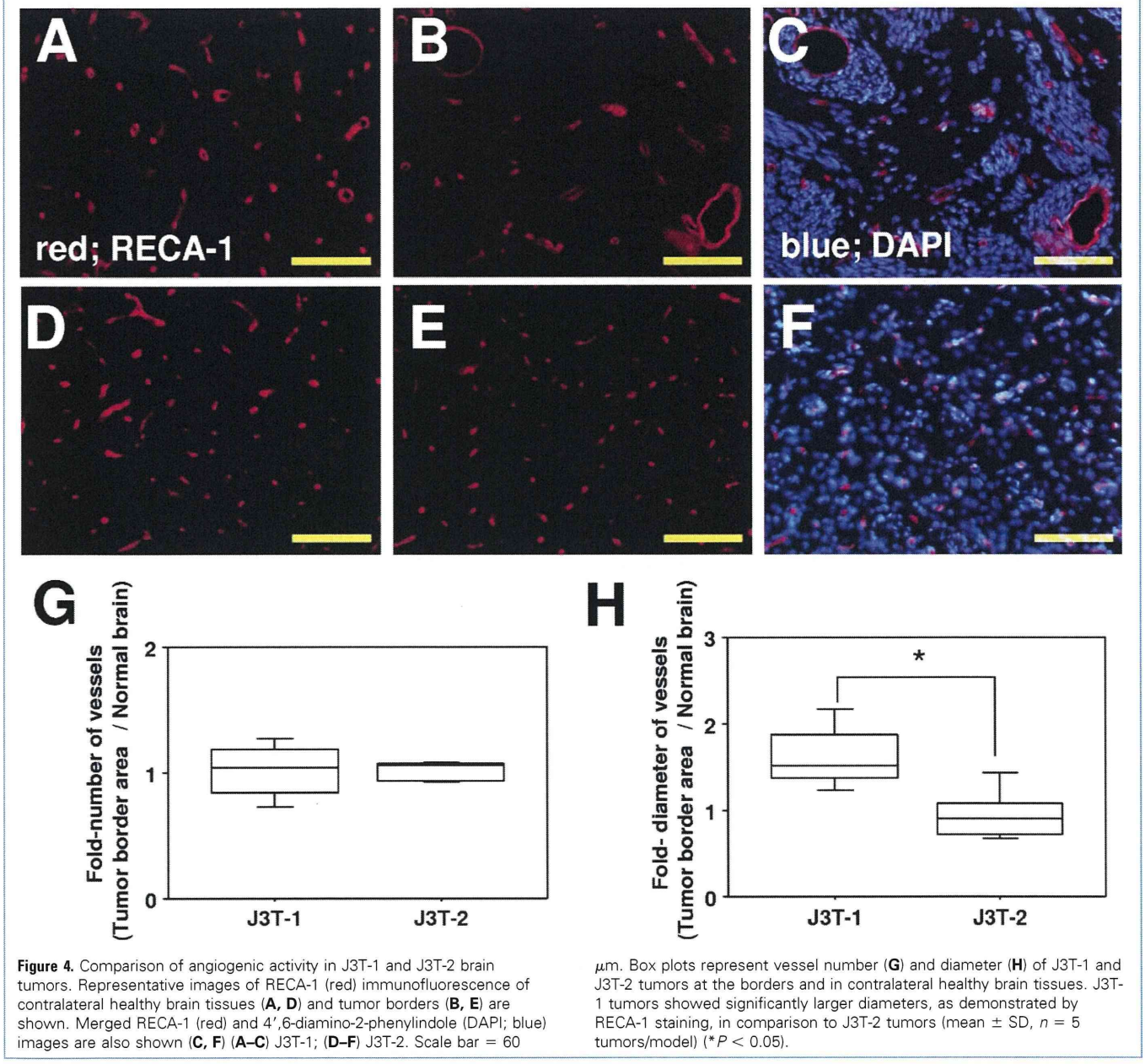

Figure 4. Comparison of angiogenic activity in J3T-1 and J3T-2 brain tumors. Representative images of RECA-1 (red) immunofluorescence of contralateral healthy brain tissues (**A, D**) and tumor borders (**B, E**) are shown. Merged RECA-1 (red) and 4′,6-diamino-2-phenylindole (DAPI; blue) images are also shown (**C, F**) (**A–C**) J3T-1; (**D–F**) J3T-2. Scale bar = 60 μm. Box plots represent vessel number (**G**) and diameter (**H**) of J3T-1 and J3T-2 tumors at the borders and in contralateral healthy brain tissues. J3T-1 tumors showed significantly larger diameters, as demonstrated by RECA-1 staining, in comparison to J3T-2 tumors (mean ± SD, $n = 5$ tumors/model) ($^*P < 0.05$).

elinated axons in the corpus callosum and cortex. No dilated blood vessels or clusters of tumor cells were seen in areas of the tumor distant from the center. Similar models showing diffuse infiltration of glioma cells are rare. Recently, several investigative groups (2, 35, 40) have established diffusely invading gliomas from human glioma samples. They also showed that such tumor models lack angiogenesis (35). In human samples, we found that most of the single cells did not seem to form clusters or did not adhere to distant vasculature. Few reports have referred to the infiltrative growth pattern of tumor cells following myelinated axons in histopathologic examination of human malignant glioma samples (3, 18, 41). Bernsen et al. (7) reported the complete absence of angiogenesis in samples of gliomatosis cerebri, which is an extreme example of such diffuse infiltrative growth of glial tumors. Therefore, this invasive phenotype was angiogenesis independent and the foothold of tumor cells is mainly along myelinated axons (**Figure 10B**). By comparative profiling, we have shown that integrin $\alpha v\beta 3$, MMP-2, nestin, and SPARC were overexpressed in J3T-2 cells than in J3T-1 cells. Integrin $\alpha v\beta 3$ is expressed by tumor cells at the invasive edge of the tumor (3, 4). MMP-2 is known to be important in the invasive properties of neoplastic cells (3). The interaction of integrin $\alpha v\beta 3$ with one of its ligands, vitronectin, may contribute to invasion by regulating the activation of proteases, including MMP-2 (3, 4, 12). SPARC promotes brain tumor invasion in vivo and in in vitro study (42). MMP-2 expression is up-regulated by SPARC using

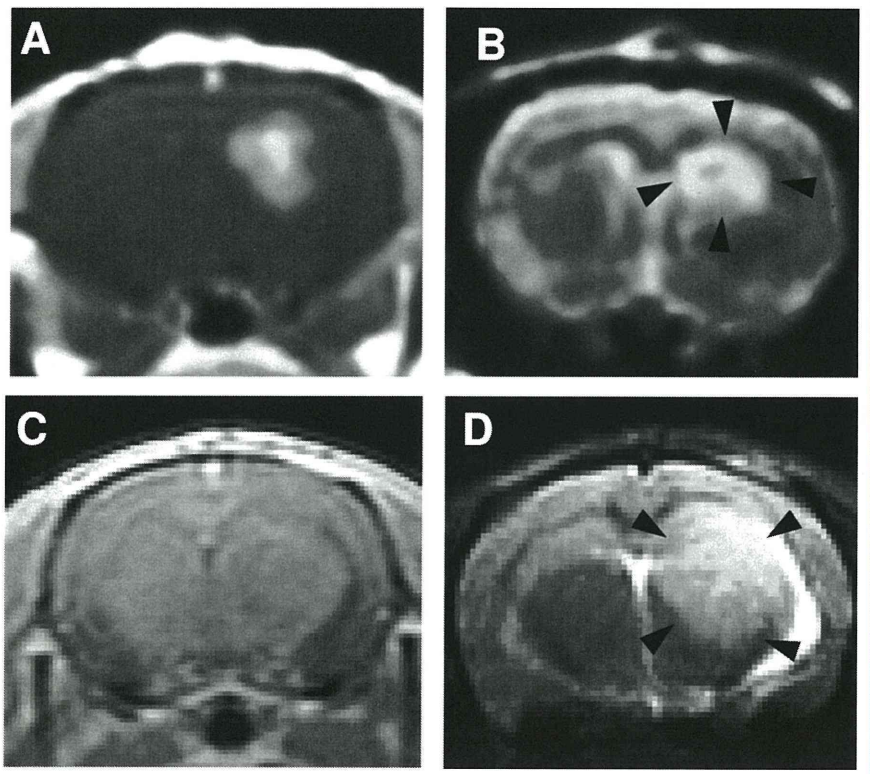

Figure 5. Magnetic resonance imaging coronal view of rat brains at the level of the largest lesion diameter. (**A**) Gadolinium-diethylenetriaminepenta-acetic acid (Gd-DTPA)-enhanced T_1-weighted image of a rat J3T-1 tumor. (**B**) T_2-weighted image of a rat J3T-1 tumor. (**C**) Gd-DTPA-enhanced T_1-weighted image of a rat J3T-2 tumor. (**D**) T_2-weighted image of a rat J3T-2 tumor. Note that the diffuse high signal intensity area (arrowheads) is depicted in both tumors on T_2-weighted images (**B, D**); however, remarkable enhancement with Gd-DTPA is seen only for J3T-1 tumors (**A**) and not for J3T-2 tumors (**C**).

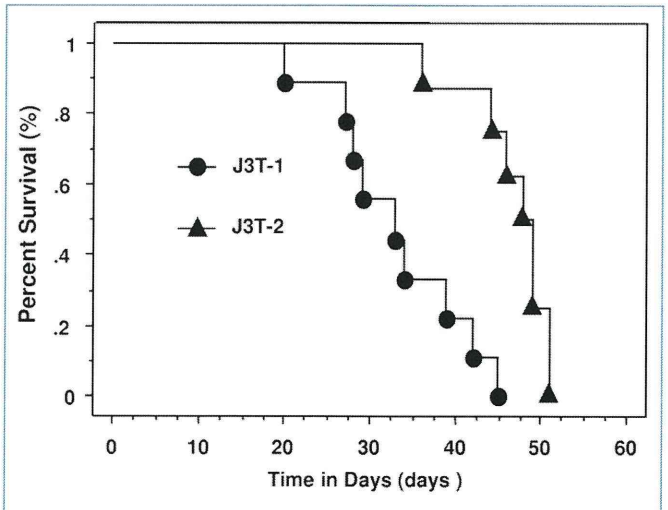

Figure 6. Kaplan-Meier survival of athymic mice inoculated with J3T-1 or J3T-2 cells. All athymic mice inoculated with J3T-1 cells (n = 9) and J3T-2 cells (n = 8) died because of brain tumor progression. Mean survival of mice with J3T-1 brain tumor was 33 days and that of mice with J3T-2 tumor was 48 days. The survival time of J3T-2 tumor mice was significantly higher (P = 0.0004, log-rank test).

cDNA array analysis in U87T2 and A2b2 clones (19). Nestin is an intermediate filament protein, commonly used as a marker for undifferentiated cells in the developing CNS and for CNS tumors. Kitai et al. (29) reported that nestin is a useful marker for examining the infiltration of malignant astrocytic cells into surrounding tissue.

Results from MRI studies support the interpretation of the angiogenic status of the two animal models. In human malignant glioma, gadolinium enhancement was seen in the main mass where the blood-brain barrier (BBB) of neovascular vessels was disrupted. Diffuse astrocytoma or gliomatosis cerebri were characterized by diffuse high intensity lesions on T_2-weighted images and absence of enhancement on T_1-weighted images. The diffuse invasive area around the enhancing mass of a malignant glioma was also depicted as high intensity on T_2-weighted images (47). Therefore, angiogenesis was observed only in J3T-1 tumors that showed gadolinium enhancement due to BBB disruption, and not in J3T-2 tumors.

Histopathologic examination of the experimental animal models and human glioblastoma samples confirmed that there were at least two invasive and angiogenic phenotypes, namely angiogenesis-dependent and angiogenesis-independent invasion. Therefore, angiogenesis was an important factor contributing to the regulation of patterns of invasion.

Examination of human tumor samples demonstrated that malignant astrocytoma and glioblastoma consisted of a mixture of subclones that showed angiogenesis-dependent and angiogenesis-independent invasion in various proportions. In addition, gliomatosis cerebri is an extreme example of a tumor developed solely by subclones that show angiogenesis-independent invasion.

Importance of Both Invasion and Angiogenesis as Targets in Treating Malignant Gliomas

Currently available therapeutic agents for malignant glioma are mostly antiproliferative and antiangiogenic agents.

Antiproliferative drugs can be delivered to tumor cells in the center and at the margins of tumors through BBB-disrupted neovascular vessels; however, most drugs cannot reach diffusely infiltrating tumor cells